

Volume-of-Fluid computational foundation for variable-density, two-phase, supercritical-fluid flows

Jordi Poblador-Ibanez^{1,*}, William A. Sirignano²

University of California, Irvine, CA 92697-3975, United States

Abstract

A two-phase, low-Mach-number flow solver is proposed for compressible liquid and gas with phase change. The interface is tracked using a split Volume-of-Fluid method, which solves the advection of the reference phase (i.e., liquid). This split advection method is generalized for the case where the liquid velocity is not divergence-free and both phases exchange mass across the interface, as happens at near-critical and supercritical pressure conditions. In this thermodynamic environment, the dissolution of lighter gas species into the liquid phase is enhanced and vaporization or condensation can occur simultaneously at different locations along the liquid-gas interface. A sharp interface is identified by using a Piecewise Linear Interface Construction (PLIC). Mass conservation to machine-error precision is achieved in the limit of incompressible liquid, but not with the liquid compressibility and mass exchange.

The numerical cost of solving two-phase, supercritical flows is very high because: a) local phase equilibrium is imposed at each interface cell to determine the interface solution (e.g., temperature, composition); b) a complete thermodynamic model is used to obtain fluid properties everywhere; and c) phase-wise values for certain variables (i.e., velocity) are obtained via extrapolation techniques. Furthermore, the Volume-of-Fluid method and the PLIC add extra computational costs to any two-phase flow solver. To alleviate this numerical cost, the pressure Poisson equation (PPE) is split into a constant-coefficient implicit part and a variable-coefficient explicit part. Thus, a Fast Fourier Transform (FFT) method can be used for the PPE, which directly solves the continuity constraint to machine-error precision.

Various validation tests are performed to show the accuracy and viability of the present approach. Then, the growth of surface instabilities in a binary system composed of liquid *n*-decane and gaseous oxygen at supercritical pressures for *n*-decane are analyzed. Other features of supercritical liquid injection are also shown.

Keywords: supercritical pressure, phase change, phase equilibrium, atomization, volume-of-fluid, low-Mach-number compressible flow

*Corresponding author

Email address: poblador@uci.edu (Jordi Poblador-Ibanez)

¹Graduate Student Researcher, Department of Mechanical and Aerospace Engineering.

²Professor, Department of Mechanical and Aerospace Engineering.

1. Introduction

An interest in achieving elevated operating pressures exists in engineering applications involving chemical combustion of fuels (e.g., gas turbines, liquid propellant rockets). Optimization of combustion efficiency and energy conversion per unit mass of fuel points to the design of high-pressure combustion chambers. Some examples include diesel or gas turbine engines, which operate in the range of 25 to 40 bar, or rocket engines, whose operating pressures range from 70 to 200 bar. Moreover, the mixing process of the fuel with the surrounding oxidizer, as well as its vaporization in the case of liquid fuels, also dictates the overall performance of the combustion process.

Understanding the physics behind the mixing process of a liquid fuel (i.e., atomization and vaporization) is crucial to design properly the combustion chamber size, the injectors' shape and distribution, etc. Many experimental and numerical studies addressing this issue have been performed at subcritical pressures. In this thermodynamic state, liquid and gas are easily identified and both fluids can be approximated as incompressible fluids (except in transonic or supersonic regimes). However, well-known fuels such as diesel fuel, Jet-A or RP-1 are based on hydrocarbon mixtures whose critical pressures are in the 20-bar range. Thus, actual operating conditions occur at near-critical or supercritical pressures for the liquid fuel.

Experimental studies performed at these very high pressures show the existence of a thermodynamic transition where the liquid and gas become difficult to identify: both phases present similar properties near the liquid-gas interface, which is rapidly affected by turbulence while being immersed in a variable-density layer [1–6]. Therefore, this behavior has often been described in the past as a very fast transition of the liquid to a gas-like supercritical state, neglecting any role of two-phase interface dynamics [7, 8]. Nevertheless, evidence of a two-phase behavior at supercritical pressures exist based on requirements that liquid and gas should be in local thermodynamic equilibrium (LTE) at the interface [9–13].

The observations from experiments at supercritical pressures (i.e., presence of a gas-like turbulent jet) are consistent with a fast atomization caused by the extreme environment and the failure of the experimental techniques to accurately capture liquid structures. Because liquid and gas look more alike near the interface, surface tension forces are reduced and liquid viscosities present gas-like values [14, 15]. Therefore, the interface may be subject to rapid growth of small surface instabilities and fast distortion, which can cause early breakup of very small droplets. Although some progress is being made towards new experimental techniques to capture the two-phase behavior in supercritical pressure environments [16–19], traditional methods relying on visual techniques (e.g., shadowgraphy) might suffer from scattering and refraction issues due to the presence of a cloud of small droplets submerged in a variable-density fluid. Numerical results of incompressible liquid round jets and planar sheets under conditions similar to those found at supercritical pressures support this reasoning [20–24].

At supercritical pressures, diffusion layers with strong variations of fluid properties grow on both sides of the interface. To maintain phase equilibrium at the interface, the lighter gas species dissolution into the liquid is enhanced. Thus, mixture critical properties will also change near the interface and, in general, the mixture critical pressure will be above the chamber pressure [13]. Dahms and Oefelein [25–27] have shown that at supercritical pressures the interface presents a diffuse region of a few nanometers thickness whenever the interface temperature nears the mixture critical temperature. At lower interface temperatures, phase equilibrium is well established and diffusion layers of the order of micrometers quickly form around the interface [13, 28, 29]. Similar to compressive shocks in compressible flows, which are treated as discontinuities, here the interface can be considered a discontinuity under LTE with a jump in fluid properties across it. Note that the non-equilibrium layer thickness for a shock is at least an order of magnitude greater than the phase non-equilibrium transition region.

The intrinsic complexity of supercritical fluids presents a challenge to the scientific community. A modeling and numerical framework is needed to address the injection of liquid fuel at supercritical pressures. Evidence points to a two-phase behavior of the atomization process, at least at the liquid-core level. It may be possible that small droplets do experience a transition to a supercritical fluid state. Some of the challenges include: a) the non-ideal fluid behavior at supercritical states must be captured via a thermodynamic model [14, 30] (e.g., a real-gas equation of state); b) LTE governs the state of the liquid-gas interface, while heat and mass transfer occur across it. Moreover, the interface should be treated as a sharp discontinuity, where fluid properties such as density or viscosity are discontinuous, as well as the heat fluxes and concentration gradients into the interface; c) the interface location must be properly tracked; and d) a computationally efficient method is desired since the additional requirements to solve supercritical flows are costly.

Various interface tracking methods exist, such as the Level-Set (LS) method by Sussman et al. [31, 32] and Osher and Fedkiw [33] and the Volume-of-Fluid (VOF) method [34, 35]. A more extensive review on interface tracking methods can be found in [36]. The LS method has been widely used in the literature. It tracks a distance function to the interface and a sharp representation can be achieved by combining it with a ghost fluid method (GFM) [37, 38]. However, the GFM applied to compressible non-ideal fluids at supercritical pressures is not straightforward and the LS method suffers from numerical mass loss. That is, numerical errors in both the advection of the LS and the reinitialization of the distance function artificially displace the interface. This problem worsens in high-curvature regions relative to the mesh size. Therefore, it becomes difficult to address this issue in atomization simulations. Even when discretizing the LS transport equation with high-order numerical schemes (e.g., WENO) or using the more accurate Gradient Augmented Level-Set method [39], some degree of mass loss exists.

On the other hand, VOF methods that conserve mass to machine-error precision exist [40]. The VOF method tracks the volume occupied by the reference phase (i.e., the liquid) in all computational cells and it handles vaporization or condensation naturally. The governing equations are solved with a sharp interface

approach that only diffuses the interface in a region of the order of $O(\Delta x)$ by volume-averaging fluid properties at interface cells [41, 42]. This is a better option than other diffuse-interface approaches based on the LS method, which impose an interface numerical thickness of $O(3\Delta x)$ that can overlap with the actual diffusion layers [31–33]. Therefore, the VOF method is preferred here.

VOF methods such as those developed by Baraldi et al. [40], Dodd and Ferrante [41] and Dodd et al. [42] are good starting points to develop numerical tools for supercritical atomization. Even though these works are developed for incompressible liquids with or without phase change, they are computationally efficient and present a mass-conserving, sharp interface tracking. Extending the methodologies presented in [40–42] to handle compressible two-phase flows coupled with real-gas thermodynamics provides an efficient numerical tool to study supercritical liquid injection. Few works address the extension of VOF methods to compressible liquids [43, 44], much less address the non-ideal thermodynamics at high pressures. Therefore, a clear gap in the literature needs to be filled.

The authors are aware of other works and methods to solve compressible two-phase flows. However, they don't satisfy the main goals the present work aims to achieve. They often present complex interface tracking algorithms and are computationally expensive, even before coupling any thermodynamic model to resolve the fluid states and the interface LTE solution.

In this paper, a numerical methodology to solve low-Mach-number, compressible two-phase flows at supercritical pressures is introduced. The necessary governing equations are presented in Section 2 and a summary of the thermodynamic model used to represent non-ideal fluids is presented in Section 3. In Section 4, we extend the VOF method from Baraldi et al. [40] to track compressible liquids with phase change. The main bulk of the numerical approach and algorithm to solve the governing equations is presented in Section 5. To ease the computational cost, the pressure-correction method by Dodd and Ferrante [41] and Dodd et al. [42] for incompressible flows is extended to low-Mach-number flows with phase change. Thus, a FFT method can be used to solve the PPE. Finally, Section 6 presents some test problems to validate the methodology and determine its viability to simulate liquid injection at supercritical pressures.

2. Governing equations

The governing equations of fluid motion for compressible two-phase flows are the continuity equation

$$\frac{\partial \rho}{\partial t} + \nabla \cdot (\rho \vec{u}) = 0 \quad (1)$$

and the momentum equation

$$\frac{\partial}{\partial t}(\rho \vec{u}) + \nabla \cdot (\rho \vec{u} \vec{u}) = -\nabla p + \nabla \cdot \bar{\tau} \quad (2)$$

where ρ and \vec{u} are the fluid density and velocity, respectively, and p is the dynamic pressure. $\bar{\tau} = \mu[\nabla \vec{u} +$

$\nabla \bar{\mathbf{u}}^T - \frac{2}{3}(\nabla \cdot \bar{\mathbf{u}})\bar{\mathbf{I}}$ is the viscous stress dyad, where μ represents the dynamic viscosity of the fluid and $\bar{\mathbf{I}}$ represents the identity dyad. For simplicity, a Newtonian fluid under Stokes' hypothesis is assumed.

Fluid behavior is far from ideal at very high pressures, where both liquid and gas are very dense fluids and compressible. Thus, models to estimate the bulk viscosity or second coefficient of viscosity should be considered [45]. In future works, the use of the Stokes' hypothesis might be revised. A comparison with the current fluid modeling will shed more light into the issue.

Furthermore, governing equations for the species concentration and for the energy of the fluid are needed. For a binary mixture, only one species continuity equation is required. As shown in Section 6, the liquid phase begins as a pure hydrocarbon (i.e., $Y_2 = Y_F = 1$) while the gas phase initially is pure oxygen (i.e., $Y_1 = Y_O = 1$). Choosing the oxidizer species, where $\sum_{i=1}^{N=2} Y_i = Y_O + Y_F = 1$, its governing equation is

$$\frac{\partial}{\partial t}(\rho Y_O) + \nabla \cdot (\rho Y_O \bar{\mathbf{u}}) = \nabla \cdot (\rho D_m \nabla Y_O) \quad (3)$$

Here, a mass-based Fickian diffusion coefficient, D_m , is chosen to model the diffusion flux due to concentration gradients. Thermo-diffusion (i.e., Soret effect) is neglected. Although a high pressure model is used to estimate this transport coefficient (see Section 3), the use of more complex models to evaluate mass diffusion will be investigated in the future.

The energy equation is written as an enthalpy transport equation as

$$\frac{\partial}{\partial t}(\rho h) + \nabla \cdot (\rho h \bar{\mathbf{u}}) = \nabla \cdot \left(\frac{\lambda}{c_p} \nabla h \right) + \sum_{i=1}^{N=2} \nabla \cdot \left(\left[\rho D_m - \frac{\lambda}{c_p} \right] h_i \nabla Y_i \right) \quad (4)$$

where h is the mixture specific enthalpy, λ is the thermal conductivity and c_p is the specific heat at constant pressure. Due to the low-Mach-number configuration analyzed in this work, pressure gradient terms, temporal variations of pressure and viscous dissipation have been neglected. The substitution $\lambda \nabla T = (\lambda/c_p) \nabla h - \sum_{i=1}^{N=2} (\lambda/c_p) h_i \nabla Y_i$ is made and, for a non-ideal fluid, the fact that the mixture enthalpy is not exactly equal to the weighted sum of partial enthalpies (i.e., $h \neq \sum_{i=1}^{N=2} Y_i h_i$) is also considered in Eq. (4) for the mixture enthalpy. Nevertheless, the term related to energy transport via mass diffusion is modeled using the partial enthalpy, h_i , to evaluate the partial derivative of enthalpy with respect to mass fraction. Fickian diffusion is still considered.

2.1. Interface matching relations

The solution of the governing equations is continuous within each phase. However, a discontinuity in thermodynamic and transport properties exists across the interface. Thus, interface matching relations must be defined and embedded into the solution of the governing equations. This section defines such relations, while Section 5 addresses the integration of these matching relations into the solution of the governing equations.

The interface, denoted by Γ , separates the liquid and gas domains. The subscripts l and g refer to the liquid phase and the gas phase, respectively. The normal and tangential unit vectors at any interface location are represented by \vec{n} and \vec{t} , respectively. With \vec{n} defined positive pointing towards the gas phase, the mass flux per unit area across the interface, \dot{m}' , is positive when vaporization occurs and negative when condensation occurs.

The vaporization or condensation rate is computed from

$$\dot{m}' = \rho_l(\vec{u}_l - \vec{u}_\Gamma) \cdot \vec{n} = \rho_g(\vec{u}_g - \vec{u}_\Gamma) \cdot \vec{n} \quad (5)$$

where \vec{u}_Γ is the interface velocity which can vary along the interface.

If \dot{m}' is non-zero, then the interface moves with respect to the fluid. In this case, the normal component of the velocity field is discontinuous across the interface while the tangential component is continuous. These conditions are given by

$$(\vec{u}_g - \vec{u}_l) \cdot \vec{n} = \left(\frac{1}{\rho_g} - \frac{1}{\rho_l} \right) \dot{m}' \quad ; \quad \vec{u}_g \cdot \vec{t} = \vec{u}_l \cdot \vec{t} \quad (6)$$

A pressure jump across the interface is caused by a combination of surface tension force, mass exchange across the interface and a mismatch in the normal viscous stresses, as seen in Eq. (7). σ represents the surface tension coefficient and κ is the interface curvature, defined positive with a convex liquid shape (i.e., $\kappa = \nabla \cdot \vec{n}$).

$$p_l - p_g = \sigma \kappa + (\vec{\tau}_l \cdot \vec{n}) \cdot \vec{n} - (\vec{\tau}_g \cdot \vec{n}) \cdot \vec{n} + \left(\frac{1}{\rho_g} - \frac{1}{\rho_l} \right) (\dot{m}')^2 \quad (7)$$

Because the interface properties may vary along the interface, the shear stress across the interface will not be continuous in the presence of a surface tension coefficient gradient. The tangential stress balance is given by

$$(\vec{\tau}_g \cdot \vec{n}) \cdot \vec{t} - (\vec{\tau}_l \cdot \vec{n}) \cdot \vec{t} = \nabla_s \sigma \cdot \vec{t} \quad (8)$$

where $\nabla_s = \nabla - \vec{n}(\vec{n} \cdot \nabla)$ is the surface gradient. While the normal force $\sigma \kappa$ in Eq. (7) tends to minimize surface area and smooth the liquid surface in two-dimensional structures, the surface tension coefficient gradient along the interface drives the flow toward regions of higher surface tension coefficient.

Matching conditions for the species continuity equation and the energy equation become, respectively,

$$\dot{m}'(Y_{O,g} - Y_{O,l}) = (\rho D_m \nabla Y_O)_g \cdot \vec{n} - (\rho D_m \nabla Y_O)_l \cdot \vec{n} \quad (9)$$

and

$$\dot{m}'(h_g - h_l) = \left(\frac{\lambda}{c_p} \nabla h \right)_g \cdot \vec{n} - \left(\frac{\lambda}{c_p} \nabla h \right)_l \cdot \vec{n} + \left[\left(\rho D_m - \frac{\lambda}{c_p} \right) (h_O - h_F) \nabla Y_O \right]_g \cdot \vec{n} - \left[\left(\rho D_m - \frac{\lambda}{c_p} \right) (h_O - h_F) \nabla Y_O \right]_l \cdot \vec{n} \quad (10)$$

where the energy matching equation has been simplified for a binary-mixture configuration.

Phase-equilibrium relations provide a necessary thermodynamic closure for the interface matching. That is, local thermodynamic phase equilibrium is imposed through an equality in chemical potential for each species on both sides of the interface. This condition can be expressed in terms of an equality in fugacity [46, 47], f_i , as

$$f_{li}(T_l, p_l, X_{li}) = f_{gi}(T_g, p_g, X_{gi}) \quad (11)$$

where fugacity is a function of temperature, pressure and mixture composition. From a thermodynamic point of view, the pressure jump across the interface due to surface tension is negligible and pressure is treated constant and equal to the chamber value for phase equilibrium purposes (i.e., $p_l \approx p_g \approx p_{ch}$). As explained later in Section 5, the thermodynamic pressure is assumed to be constant for low-Mach-number compressible flows and dynamic pressure variations are related to fluid motion but have little effect on fluid properties. Under this assumption, phase equilibrium can be expressed using the fugacity coefficient, $\Phi_i \equiv f_i/pX_i$, as $X_{li}\Phi_{li} = X_{gi}\Phi_{gi}$ where X_i represents the mole fraction of species i .

Furthermore, the interface presents a negligible thickness of the order of nanometers [25, 26] while mass, momentum and energy quickly diffuse within regions of the order of micrometers around the interface [13, 28, 29]. Thus, the interface thickness is neglected in the present work and temperature is assumed continuous (i.e., $T_g = T_l = T_I$).

The continuous temperature assumption simplifies the solution of phase equilibrium and a mixture composition can readily be obtained on each side of the interface. The plausibility of this interface modeling is valid as long as the equilibrium solution is far from the mixture critical point [27] and the interface thermal resistivity is negligible [48], which is true even for the small thermal conductivities observed at the interface. The thermodynamic states expected in the problem configurations analyzed in this work are sufficiently far from the mixture critical point as reported in Poblador-Ibanez and Sirignano [13].

3. Thermodynamic model

The thermodynamic model implemented in this work is based on a volume-corrected Soave-Redlich-Kwong (SRK) cubic equation of state [49], which is able to represent non-ideal fluid states for both the gas and liquid phases. The original SRK equation of state [46] presents density errors of up to 20% when compared to experimental measurements whenever a dense fluid is being predicted [14, 50] (i.e., liquid or high pressure gas). The volume-corrected SRK equation of state is expressed in terms of the compressibility factor, Z , as

$$Z^3 + (3B_* - 1)Z^2 + [B_*(3B_* - 2) + A - B - B^2]Z + B_*(B_*^2 - B_* + A - B - B^2) - AB = 0 \quad (12)$$

with

$$Z = \frac{p}{\rho RT} \quad ; \quad A = \frac{a(T)p}{R_u^2 T^2} \quad ; \quad B = \frac{bp}{R_u T} \quad ; \quad B_* = \frac{c(T)p}{R_u T} \quad (13)$$

The parameters of this equation of state are: $a(T)$, which is a temperature-dependent cohesive energy parameter; b , which represents a volumetric parameter related to the space occupied by the molecules; and $c(T)$, which is a temperature-dependent volume correction. R and R_u are the specific gas constant and the universal gas constant, respectively. The solution of this cubic equation provides the density of the fluid mixture, ρ . Furthermore, its implementation is efficient since analytical expressions exist to find the solution of a cubic equation and there is no need to develop an iterative time-consuming solver.

The volume-corrected SRK equation of state is used, together with high-pressure correlations, to evaluate fluid properties and transport coefficients (e.g., viscosity) [47, 51, 52]. For low-Mach-number compressible flows, pressure is assumed uniform and equal to the thermodynamic or ambient pressure. Further details on the development and practical implementation of this thermodynamic model can be found in Davis et al. [28] and the respective references mentioned in this section.

4. Interface model

The accurate solution of the location and properties of the interface separating two immiscible fluids is of utmost importance in a two-phase fluid solver. In this work, a compressible extension of the VOF method is used to track the interface (Section 4.1) and evaluate its geometrical properties (Section 4.2). At high pressures, the dissolution of lighter gas species into the liquid phase is enhanced, thus causing the liquid volume to locally expand near the interface. Moreover, phase change is an important feature of high-pressure environments, where vaporization or condensation can occur simultaneously at different locations along the interface. This behavior depends on the local thermodynamic phase equilibrium and the balancing of the mass, momentum and energy fluxes at the liquid-gas interface, as shown in Section 2.1.

4.1. The Volume-of-Fluid method for compressible liquids

The VOF method [34, 35] tracks a characteristic function, $\chi(\vec{x}, t)$, which is advected by the fluid velocity, \vec{u} , following Eq. (14). $\chi = 1$ in the reference phase (i.e., liquid phase in the present work) and $\chi = 0$ in the other phase (i.e., gas phase).

$$\frac{D\chi}{Dt} = \frac{\partial \chi}{\partial t} + \vec{u} \cdot \nabla \chi = 0 \quad (14)$$

The volume fraction, C , represents the volume occupied by the reference fluid in a cell with respect to the total cell volume, V_0 . That is,

$$C = \frac{1}{V_0} \iiint_{V_0} \chi dV \quad (15)$$

The advection of Eq. (14) is performed using the algorithm and VOF tools proposed in Baraldi et al. [40]. A three-step split advection algorithm is implemented, consisting of an Eulerian Implicit, an Eulerian Algebraic and a Lagrangian Explicit steps (EI-EA-LE algorithm). Details about this algorithm and its extension to compressible liquids are explained in the following paragraphs and shown in Eqs. (19), (20) and (21).

Compared to the original EI-EA-LE method proposed by Scardovelli et al. [53], the algorithm presented in [40] is wisp-free and mass-conserving to machine-error precision for incompressible flows. Yet, numerical errors exist and are bounded by the accuracy to which $\nabla \cdot \vec{u} = 0$ is satisfied and other errors introduced by the geometrical operations of the VOF method.

During the split advection of Eq. (14), the interface is geometrically reconstructed between steps using the PLIC method by Youngs [54]. Although the reconstruction process is computationally expensive, the method presented in [40] is more efficient than other higher-order VOF methods (e.g., 3D-ELVIRA [55]) and ensures that the volume fraction obtained by solving Eq. (14) is conserved. Therefore, mass is conserved to machine-error precision when the fluid density is constant. As reported in Haghshenas et al. [56], this is only achieved by low-order convective schemes as the one used in [40]. This low-order advection scheme causes smearing of the solution around the interface, which might introduce geometrical errors as the interface is advected by the fluid velocity. Nevertheless, in this work volume-conservation properties are favored over higher-order advection schemes and a sufficiently low CFL condition is used to limit the magnitude of these errors.

The VOF method proposed in [40] must be extended to allow for mass exchange across the interface and to a compressible formulation since the liquid volume expands as the lighter gas dissolves. The equation tracking the reference phase, Eq. (14), can be rewritten in conservative form as

$$\frac{\partial \chi}{\partial t} + \nabla \cdot (\chi \vec{u}_l) = \chi \nabla \cdot \vec{u}_l - \frac{\dot{m}}{\rho_l} \quad (16)$$

where \dot{m} is the mass flux per unit volume added to (condensation with $\dot{m} < 0$) or subtracted from (vaporization with $\dot{m} > 0$) the liquid phase, which is only non-zero at interface. \dot{m} is evaluated as $\dot{m} = \dot{m}' \delta_\Gamma$, where \dot{m}' is the mass flux per unit area across the interface and δ_Γ activates the phase-change term only at the interface cells. The value of \dot{m}' is obtained by solving the system of interface matching conditions discussed in Section 2.1 and Section 5.2. Here, δ_Γ is obtained from the concept of interfacial surface area density as given in Palmore and Desjardins [57], whereby in a given region Ω of the domain,

$$\delta_\Gamma = \frac{\int_{\Gamma \cap \Omega} dS}{\int_{\Omega} dV} \quad (17)$$

This term is non-zero only at interface cells, where $\delta_\Gamma = A_\Gamma / V_0$, with V_0 being the cell volume and A_Γ the area of the interface plane crossing the cell (i.e., from the PLIC).

Notice the use in Eq. (16) of the reference phase density, ρ_l , and a liquid phase velocity, \vec{u}_l . Because of the different fluid compressibilities and the velocity jump across the interface in the presence of phase

change (see Section 2.1), one needs to advect the liquid phase using a velocity field only representative of the liquid. Extrapolation techniques dealing with this issue are explained later in Section 5.3. For the compressible liquid, ρ_l is the interface liquid density.

Integrating Eq. (16) over the volume of the cell and in time with a first-order forward Euler scheme, an equation to update the volume fraction of a given cell is obtained as

$$C^{n+1} = C^n - \sum_{i=1}^{N_{\text{faces}}} F_i + \tilde{C}(\nabla \cdot \vec{u}_l)\Delta t - \frac{\dot{m}}{\rho_l}\Delta t \quad (18)$$

The term $\sum_{i=1}^{N_{\text{faces}}} F_i$ represents the sum of the signed fluxes of the reference phase in and out of the cell (i.e., taking into account the direction of the cell face normal unit vector pointing outwards). These fluxes are evaluated geometrically within the EI-EA-LE split advection algorithm coupled with PLIC [40]. \tilde{C} is the volume fraction of the cell, but where the choice of implicit ($\tilde{C} = C^{n+1}$) or explicit ($\tilde{C} = C^n$) evaluation could be made. However, only the implicit formulation, $\tilde{C} = C^{n+1}$ has been found to provide consistent results with the split advection method used here.

In summary, Eq. (18) accounts for the variation of the volume fraction at a given cell caused not only by convective fluxes in and out of the cell, but also by the local volume expansion of the reference phase and the volume of the reference phase added/subtracted due to phase change. In these ways, it differs from prior approaches that treated incompressible liquids without phase change.

The three-step EI-EA-LE split advection is constructed such that $C^{n+1} = C^n - \sum_{i=1}^{N_{\text{faces}}} F_i$ is recovered for an incompressible fluid without phase change. Nevertheless, the EI and LE steps consider the local non-zero divergence in the advection direction while the EA step is designed and only used to satisfy the incompressible three-dimensional version of Eq. (18). That is, in a two-dimensional code only an EI-LE split advection algorithm is needed and it already satisfies $C^{n+1} = C^n - \sum_{i=1}^{N_{\text{faces}}} F_i$ when $\nabla \cdot \vec{u}_l = 0$ and $\dot{m} = 0$. The EI-EA-LE consecutive steps update the volume fraction such that $C^n \rightarrow C^{EI} \rightarrow C^{EA} \rightarrow C^{LE} = C^{n+1}$ (or $C^n \rightarrow C^{EI} \rightarrow C^{LE} = C^{n+1}$ in two dimensions).

In the following lines, the nomenclature follows that u , v and w represent the liquid velocity components in x -, y - and z -directions and E , W , N , S , T and B define the East-West (x -direction), North-South (y -direction) and Top-Bottom (z -direction) cell faces, respectively.

For a two-dimensional compressible flow without phase change ($\dot{m} = 0$), the EI-LE steps yield, with the EI step in the x -direction and the LE step in the y -direction,

$$C^{EI} = \frac{C^n + F_W^u - F_E^u}{1 - \frac{u_E - u_W}{\Delta x} \Delta t} \quad (19a)$$

$$C^{LE} = C^{EI} \left(1 + \frac{v_N - v_S}{\Delta y} \Delta t \right) + F_S^v - F_N^v = C^n - \sum_{i=1}^{N_{\text{faces}}} F_i + C^{EI}(\nabla \cdot \vec{u}_l)\Delta t \neq C^{n+1} \quad (19b)$$

which does not immediately satisfy the form of Eq. (18). Thus, a corrective step is needed after the LE step,

as defined in Eq. (20). In a three-dimensional compressible flow, the EA step is designed such that Eq. (19) and the correction shown in Eq. (20) are still valid.

$$C^{n+1} = C^{LE} + (\tilde{C} - C^{EI})(\nabla \cdot \vec{u}_l)\Delta t \quad (20)$$

The present algorithm implements the volume addition or subtraction caused by mass exchange before advecting the interface. On a uniform mesh and with the EI step in the x -direction, the EA step in the y -direction and the LE step in the z -direction, the three advection steps shown in Baraldi et al. [40] now follow Eq. (21), including the preliminary step to address phase change and the final correction step to match the form of Eq. (18). In the code, the algorithm alternates the direction of the EI-EA-LE steps to minimize directional bias.

$$C^{PC} = C^n - \frac{\dot{m}}{\rho_l} \Delta t \quad (21a)$$

$$C^{EI} = \frac{C^{PC} + F_W^u - F_E^u}{1 - \frac{u_E - u_W}{\Delta x} \Delta t} \quad (21b)$$

$$C^{EA} = \frac{C^{EI} \left[1 - \frac{u_E - u_W}{\Delta x} \Delta t + (\nabla \cdot \vec{u}_l) \Delta t \right] + F_S^v - F_N^v}{1 + \frac{w_T - w_B}{\Delta z} \Delta t} \quad (21c)$$

$$C^{LE} = C^{EA} \left(1 + \frac{w_T - w_B}{\Delta z} \Delta t \right) + F_B^w - F_T^w \quad (21d)$$

$$C^{n+1} = C^{LE} + (\tilde{C} - C^{EI})(\nabla \cdot \vec{u}_l)\Delta t \quad (21e)$$

The definition of the EI, EA and LE steps shown in Eq. (21) ensures that the solution of the volume fraction, C , stays bounded (i.e., $0 \leq C \leq 1$) and $C = 1$ within the reference phase. However, as mentioned earlier, small errors still exist due to inaccuracies in the evaluation of geometrical fluxes and precision errors in how well the velocity field satisfies $\nabla \cdot \vec{u}_l$.

The wisp-suppression algorithm from Baraldi et al. [40] is used to limit the amount of wisps left in the domain, which are basically a result of finite precision when evaluating the geometrical fluxes required for the advection of Eq. (16) or, equivalently, Eq. (18).

The EA step (Eq. (21c)) might introduce small undershoots (i.e., $C < 0$) and overshoots (i.e., $C > 1$) in its incompressible form [40]. For compressible flow, the same problem exists. Moreover, the addition of phase change and volume expansion effects in the corrective step (Eq. (20)) may also cause undershoots and overshoots in C in interface cells where almost no liquid is present or where almost the entire cell volume is occupied by the liquid. To eliminate these issues, a redistribution algorithm following that of Baraldi et al. [40] and Harvie and Fletcher [58] is used. However, the present work adds directionality (following \vec{n}) to the redistribution algorithm whenever possible. Since the major part of the undershoots and overshoots in

C will be caused by phase change and volume expansion in the direction perpendicular to the interface, this approach becomes more consistent and preserves the interface shape better.

The authors acknowledge that this VOF method for compressible flows is not mass-conservative to machine error. The use of a volume-preserving algorithm does not ensure mass conservation when density is not constant. Thus, mass conservation will improve as the mesh is refined and a lower time step is used. This is no different than other available VOF methods for compressible flows [43, 44]. Nevertheless, two main reasons motivate the use of this approach: a) to maintain a sharp interface; and b) the method simplifies to the mass-conserving VOF method from Baraldi et al. [40] when $\nabla \cdot \vec{u} = 0$ and $\dot{m} = 0$.

4.2. Evaluation of interface geometry

The normal unit vector, \vec{n} , is evaluated using the Mixed-Youngs-Centered (MYC) method [59] and curvature is computed using an improved Height Function (HF) method [60]. The HF method is second-order accurate but presents considerable curvature errors whenever the normal unit vector of the interface is not aligned with the coordinate axes [40]. This situation generates spurious velocity currents around the interface which are not related to any physical process. The magnitude of these curvature errors can be limited below 1% for a sufficiently fine mesh (e.g., 32 cells per diameter in a sphere [40]).

This issue is a reason for caution in liquid injection problems where the growth of instabilities along the liquid-gas interface must be only related to physical phenomena. This problem is more important at supercritical pressures where the liquid and gas phases look more alike near the interface. In this case, the surface tension force that would stabilize these numerical instabilities caused by spurious currents is reduced.

Efforts have been made to develop more accurate methods to evaluate the interface geometry in the VOF framework. For instance, Popinet [61] presents an adaptative scheme to enhance the accuracy of curvature computations for under-resolved interfaces using the HF method. This modification to the HF method is not implemented in the present work, but it is definitely something to look at in the future. Other works combine the VOF and LS methods to use the smoother LS distribution to obtain a better estimate of the interface geometry [62, 63]. However, a key step whereby the LS function is re-distanced with respect to the PLIC interface reconstruction does not ensure a mesh-converging curvature. Together with the intrinsic complexity of combining the VOF and LS methods, the HF method is preferred in this work to evaluate curvature.

5. Numerical solution of the governing equations

The main algorithm steps at every time step are shown as a flowchart in Figure 1. The goal here is to provide some context on the necessary steps to solve the governing equations before proceeding with the individual details.

The simulation is initialized by assigning initial conditions to all variables involved in the solution process. First, the bulk of the VOF method is used, which includes the interface advection, the PLIC interface reconstruction and the algorithm to evaluate the interface curvature using the HF method. Once the interface has been updated at t^{n+1} , the governing equations for species continuity and energy are solved.

Once the entire domain has an updated solution for the interface location and its geometry, as well as the mass fraction and enthalpy on both sides, the LTE and jump conditions can be solved at each interface cell. At the same time, since the thermodynamic model only depends on the thermodynamic pressure at this low-Mach-number configurations, the fluid properties can be updated everywhere. (e.g., ρ^{n+1}).

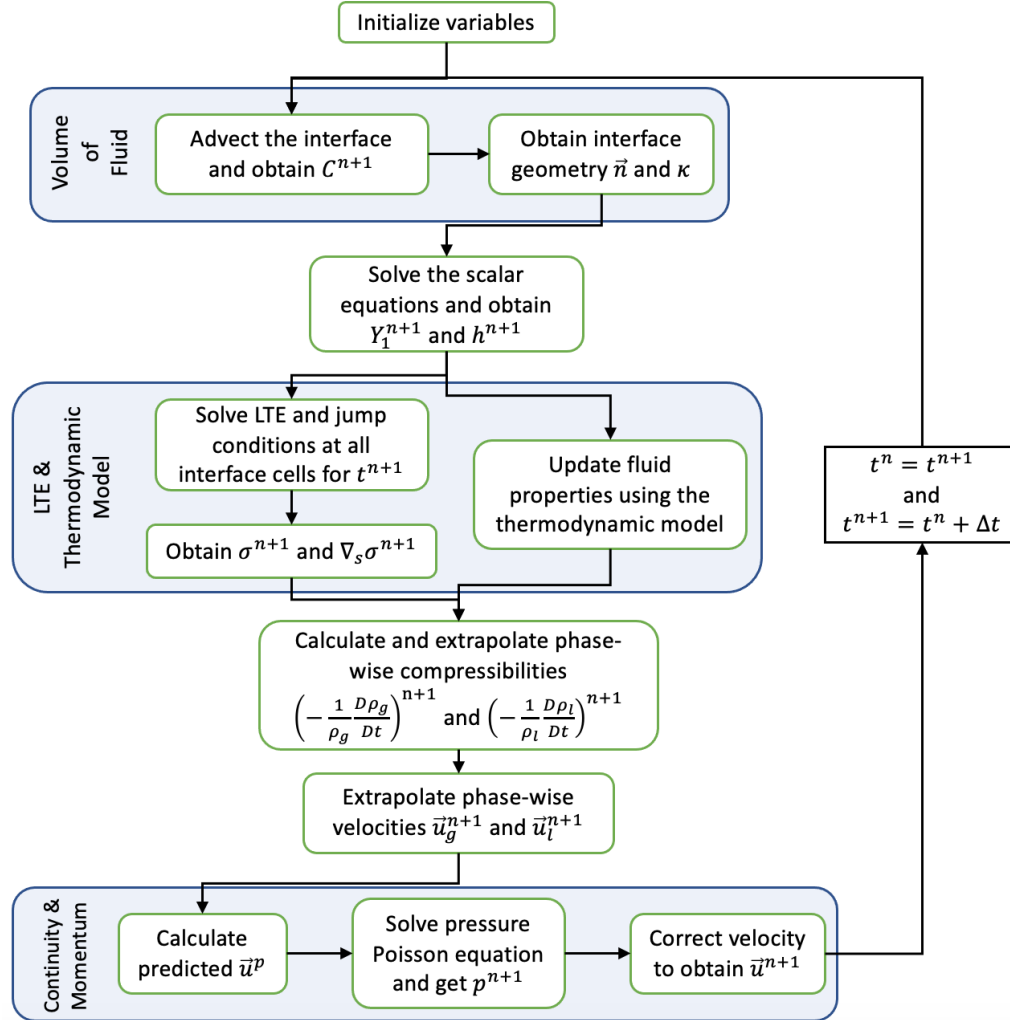


Figure 1: Algorithm flowchart of steps taken at every time step to solve low-Mach-number, two-phase flows at supercritical pressures.

Before solving the continuity and momentum equations, the new fluid compressibilities are calculated and extrapolated. After that, the phase-wise velocities are obtained from the extrapolated fluid compressibilities and are used at the next time step. Then, a predictor-projection method is used to solve the momentum

equation, which splits the pressure gradient to solve a PPE using a FFT methodology.

The VOF methodology has been presented in Section 4. The following sections address the rest of the main block of the solution algorithm in order. Section 5.1 discusses how the governing equations for the scalar variables (i.e., species continuity and energy) are solved. Then, the methodology to obtain the interface properties is presented in Section 5.2 and the evaluation of fluid compressibilities, as well as the extrapolation techniques used to obtain phase-wise compressibilities and velocities, are discussed in Section 5.3. The solution of the continuity and momentum equations is presented in Section 5.4, where a low-Mach-number Poisson equation for the pressure field is developed. Finally, Section 5.5 provides information on the evaluation of the time step, Δt , and some final remarks about the algorithm.

5.1. Discretization of species continuity and energy equations

The governing equations for species mass fraction (Eq. (3)) and energy (Eq. (4)) are solved differently than the continuity and momentum equations presented in Section 5.4. Here, the non-conservative forms of both equations are used and solved using finite differences instead of the finite volume method. The reasons for this are to obtain a better control on numerical stability and to directly include the interface in the numerical stencils used in various terms of the equations. Thus, these equations are solved in each phase independently and using phase-wise variables.

The non-conservative forms of Eqs. (3) and (4) are integrated in time using an explicit first-order step as

$$\frac{DY_O^{n+1}}{Dt} = \frac{Y_O^{n+1} - Y_O^n}{\Delta t} + (\vec{u}_m \cdot \nabla Y_O)^n = \frac{1}{\rho^n} \left[\nabla \cdot (\rho D_m \nabla Y_O)^n \right] \quad (22)$$

$$\frac{Dh^{n+1}}{Dt} = \frac{h^{n+1} - h^n}{\Delta t} + (\vec{u}_m \cdot \nabla h)^n = \frac{1}{\rho^n} \left[\nabla \cdot \left(\frac{\lambda}{c_p} \nabla h \right)^n + \sum_{i=1}^{N=2} \nabla \cdot \left(\left[\rho D_m - \frac{\lambda}{c_p} \right] h_i \nabla Y_i \right)^n \right] \quad (23)$$

where the convective and diffusive terms are evaluated explicitly at time n and the phase-wise velocity \vec{u}_m is used. The term \vec{u}_m is evaluated at the cell center using a linear average from cell face values.

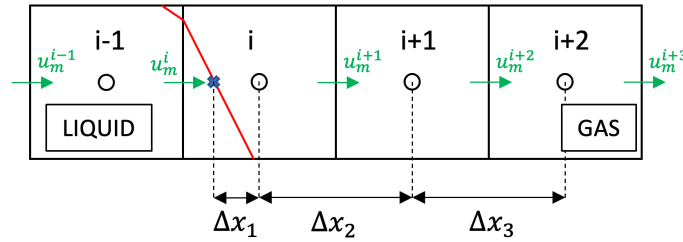


Figure 2: Sketch showing the interface intersecting the numerical stencil in the x -direction and how its location is included in the numerical discretization of the scalar equations.

The convective terms are discretized using an adaptive first-/second-order upwinding scheme to maintain numerical stability and boundedness (i.e., $Y_O \leq 1$). The physics of the problem limit the solution of the

mixture composition and temperature and, within the limits of the CFL conditions, only a first-order upwind discretization of the convective term is unconditionally bounded [64].

Figure 2 shows a sketch of a two-dimensional mesh where the interface is identified (i.e., in cells i and $i-1$). The interface can intersect the numerical stencil used to evaluate $\partial Y_O/\partial x$ depending on the cell and discretization order. Thus, $\Delta x_1 < \Delta x$ must be determined. Notice here $\Delta x_2 = \Delta x_3 = \Delta x$, being Δx the mesh size.

The PLIC interface reconstruction at cell i could be used to obtain Δx_1 . However, the approach used in Dodd et al. [42] to estimate Δx_1 is faster and more stable. The volume of liquid occupying the space between node i and $i-1$ can be used to estimate Δx_1 . That is, a staggered value of the volume fraction, $C^{i-1/2}$, is obtained from C^{i-1} and C^i , as well as from the respective PLIC interface reconstructions. Depending on the interface configuration, this approach becomes exact (i.e., equivalent to using the location obtained with the PLIC interface). Even when $C^{i-1/2} > 0$, $\Delta x_1 \neq \Delta x$ is only evaluated if nodes i and $i-1$ belong to different phases. If, in fact, the interface must be included in the numerical discretization, the interface values used in the numerical stencils are averaged similar to Eq. (44).

As an example, the discretization of ∇Y_O in the convective term $\vec{u}_m \cdot \nabla Y_O$ is shown here following the configuration presented in Figure 2. The method shown here for derivatives with respect to the x -variable will serve as templates for the derivatives with respect to y and z . For simplicity, the explicit notation has been dropped. This example covers the different scenarios that can be found when evaluating ∇Y_O and can be easily extended to other directions and interface configurations.

At cell i , the gradient using gas values is found as follows. With a uniform mesh, for $(u_m^i + u_m^{i+1})/2 < 0$ (where the phase-wise velocity is $m = g$), $\partial Y_O/\partial x$ becomes

$$\left(\frac{\partial Y_O}{\partial x}\right)^i = \begin{cases} \frac{Y_O^{i+2} - Y_O^i + (Y_O^i - Y_O^{i+1})(1 + \Delta x_3/\Delta x_2)^2}{\Delta x_2 + \Delta x_3 - \frac{(\Delta x_2 + \Delta x_3)^2}{\Delta x_2}} & \text{if second-order solution is bounded} \\ \frac{Y_O^{i+1} - Y_O^i}{\Delta x_2} & \text{if second-order solution is not bounded} \end{cases} \quad (24)$$

and if $(u_m^i + u_m^{i+1})/2 \geq 0$, it becomes

$$\left(\frac{\partial Y_O}{\partial x}\right)^i = \begin{cases} \frac{Y_O^i - Y_{O,g}^\Gamma}{\Delta x_1} & \text{if } \Delta x_1 \geq 0.05\Delta x \\ \frac{Y_O^{i+1} - Y_{O,g}^\Gamma}{\Delta x_1 + \Delta x_2} & \text{if } \Delta x_1 < 0.05\Delta x \end{cases} \quad (25)$$

where $Y_{O,g}^\Gamma$ is the gas mass fraction of species 1 at the interface. If the distance between node i and the interface is very small (i.e., $\Delta x_1 < 0.05\Delta x$), node i is skipped and the gradient is evaluated using the neighboring node $i+1$. This step becomes necessary to avoid a spike in the value of $\partial Y_O/\partial x$ when the interface is very close to the grid node, which might cause unrealistic solutions near the interface.

Another possible stencil is given in cell $i+1$ if $(u_m^{i+1} + u_m^{i+2})/2 \geq 0$. Here, $\partial Y_O/\partial x$ is evaluated as

$$\left(\frac{\partial Y_O}{\partial x}\right)^{i+1} = \begin{cases} \frac{Y_{O,g}^\Gamma - Y_O^{i+1} + (Y_O^{i+1} - Y_O^i)(-1 - \Delta x_1/\Delta x_2)^2}{-(\Delta x_1 + \Delta x_2) + \frac{(-\Delta x_1 - \Delta x_2)^2}{\Delta x_2}} & \text{if second-order solution is bounded and } \Delta x_1 \geq 0.05\Delta x \\ \frac{Y_O^{i+1} - Y_O^i}{\Delta x_2} & \text{if second-order solution is not bounded or } \Delta x_1 < 0.05\Delta x \end{cases} \quad (26)$$

where a combination of the conditions given in Eqs. (24) and (25) is used to maintain numerical stability and boundedness. Away from the interface, the upwinded gradient ∇Y_O is obtained with similar expressions as in Eqs. (24) and (26) only considering the boundedness condition.

Diffusive terms are discretized using second-order central differences, although near the interface the spatial accuracy might be reduced when including the interface. Again, we look at the discretization of $\nabla \cdot (\rho D_m \nabla Y_O)$ under the configuration presented in Figure 2. However, its extension to other directions or interface configurations is straightforward. The generic discretization of the diffusive term is

$$\frac{\partial}{\partial x} \left(\rho D_m \frac{\partial Y_O}{\partial x} \right) = \frac{(\rho D_m \partial Y_O / \partial x)^E - (\rho D_m \partial Y_O / \partial x)^W}{\Delta x} \quad (27)$$

with E and W referring to the East and West cell faces, respectively.

Fluid properties at the cell face are obtained by linear interpolation between two neighboring grid nodes. If the interface is located between the grid node and its respective cell face, the interface replaces the cell face (e.g., the West face of node i in Figure 2). Also, if the interface is located beyond a cell face but before a neighboring node, its equilibrium solution and position are used for the linear interpolation of fluid properties at the cell face and to evaluate $\partial Y_O/\partial x$ (e.g., the East face of node $i-1$ in Figure 2).

For example, the discretization of the diffusive term at cell i results in

$$\frac{\partial}{\partial x} \left(\rho D_m \frac{\partial Y_O}{\partial x} \right)^i = \frac{(\rho D_m \partial Y_O / \partial x)^E - (\rho D_m \partial Y_O / \partial x)^W}{\Delta x_1 + \Delta x_2/2} \quad (28)$$

with

$$\left(\rho D_m \frac{\partial Y_O}{\partial x} \right)^E = (\rho D_m)^E \left(\frac{Y_O^{i+1} - Y_O^i}{\Delta x_2} \right) \quad (29a)$$

$$\left(\rho D_m \frac{\partial Y_O}{\partial x} \right)^W = \begin{cases} (\rho D_m)_g^\Gamma \left(\frac{Y_O^i - Y_{O,g}^\Gamma}{\Delta x_1} \right) & \text{if } \Delta x_1 \geq 0.05\Delta x \\ (\rho D_m)_g^\Gamma \left(\frac{Y_O^{i+1} - Y_{O,g}^\Gamma}{\Delta x_1 + \Delta x_2} \right) & \text{if } \Delta x_1 < 0.05\Delta x \end{cases} \quad (29b)$$

where $(\rho D_m)^E$ is the product of the linear interpolations of ρ and D_m at the East face and $(\rho D_m)_g^\Gamma$ is the product of the interface gas values of ρ and D_m at equilibrium. Similar to the discretization of the convective term, the approximation of $\partial Y_O/\partial x$ skips node i if the interface is very close to it in order to avoid nonphysical spikes.

The discretization proposed here is at most second-order accurate in space and decreases to first order near the interface and when boundedness problems arise. Nevertheless, as stated throughout the text, stability

concerns prompt the usage of this low-order schemes. Moreover, the mesh is very fine to properly capture the interface and to obtain a smooth and converged solution of the extrapolations discussed in Section 5.3. Thus, a low-order spatial accuracy in the discretization of the scalar equations does not pose a problem.

Some special considerations are needed to ensure a stable and physically-correct solution. Two extreme cases may exist: when the interface is nearly touching the grid node (i.e., $\Delta x_1 < 0.01\Delta x$ in Figure 2) and when the node changes phase (i.e., $C^n < 0.5$ and $C^{n+1} \geq 0.5$ or $C^n \geq 0.5$ and $C^{n+1} < 0.5$). In both scenarios, the interface value of the correct phase is assigned to the grid node. If the interface displacement in Δt is very small, this approximation is reasonable. Moreover, under-resolved regions (i.e., droplets or thin areas of the order of the mesh size) might generate incorrect solutions. To avoid this problem, if a nonphysical solution is detected, the values for oxygen mass fraction or enthalpy assigned to the problematic cell are obtained from an average of the surrounding physically-correct values of the same fluid phase.

5.2. Interface local phase equilibrium and jump conditions

As discussed in Section 2.1, the interface is assumed to be in LTE. To obtain the interface equilibrium state at interface cells, the normal-probe technique is used, similar to other works [15, 42, 65]. Here, a line perpendicular to the interface plane is drawn extending into both the liquid and the gas phases. The centroid of the interface plane at a given cell is chosen as the starting point of the probe. On this line, two nodes are created per phase where the values of mass fraction and enthalpy are linearly interpolated. Thus, the normal gradients to the interface needed in Eqs. (9) and (10) can be evaluated.

Ideally, the nodes on the probe are equally spaced with Δx . However, some situations require a larger spacing to avoid using grid nodes in opposite phases when interpolating the mass fraction or the enthalpy values (see Figure 3). Since there is a sharp jump of these variables across the interface, this situation must be avoided.

In general, a second-order, one-sided, finite-difference method can be used to evaluate the perpendicular gradient at each side of the interface. To do so, the values of each variable in the two nodes on the probe and the interface value are used. Notice it is assumed that the entire interface plane has the same equilibrium solution. As the interface deforms and thin ligaments form, the normal gradients may be calculated using a first-order, one-sided finite difference method if the normal probe crosses the interface. However, at this point the mesh is poorly resolving the interface and the interface solution might become unstable.

The interface solution is unknown and an iterative process is needed to solve the system of equations formed by the jump conditions and LTE. With the simplifications introduced in this work (e.g., low-Mach-number flows, binary mixture), the interface matching relations for species continuity and energy (Eqs. (9) and (10)), together with phase equilibrium (Eq. (11)), are decoupled from the momentum matching relations (Eqs. (7) and (8)). Therefore, the same iterative solver discussed in Poblador-Ibanez and Sirignano [13] can be used to obtain the interface solution at each interface cell. This defines the properties of the interface

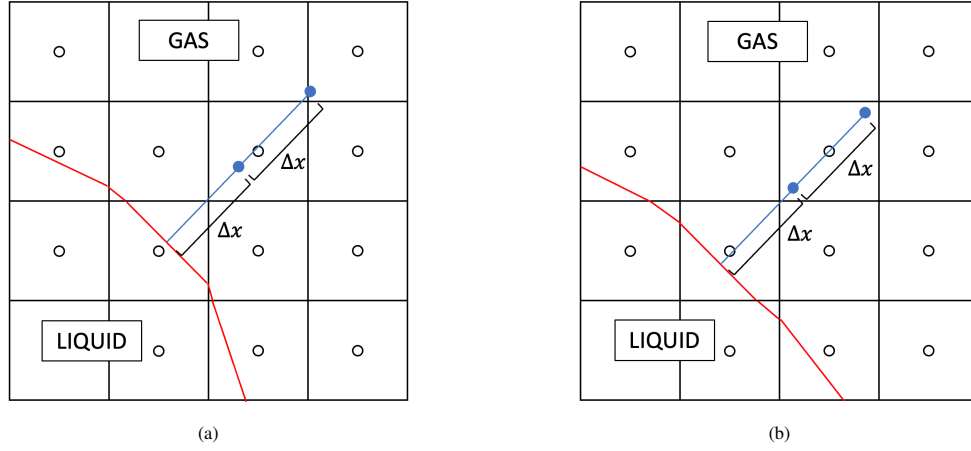


Figure 3: Construction of the normal probe used to evaluate jump conditions and LTE at the interface. For simplicity, only the probe extending into the gas phase is represented in a two-dimensional configuration. The liquid-phase normal probe is constructed in a similar manner and the extension to three dimensions is straightforward. a) Case where a constant spacing of Δx results in the probe node closest to the interface being defined by grid nodes belonging to different phases; b) Case where a constant spacing of Δx results in a well-defined probe.

plane located in a given interface cell: mass flux and heat flux across the interface, temperature, surface-tension coefficient, composition and fluid properties on each side of the interface and, in turn, the pressure jump imposed in the momentum equation.

5.3. Evaluation of fluid compressibilities and phase-wise velocity

Each phase's compressibility has to be determined in order to evaluate $\nabla \cdot \vec{u}^{n+1}$ (Eq. (40)) and solve the PPE (Eq. (43)) presented in Section 5.4. Under the low-Mach-number constraint, it is sufficient to know the density variations caused by temperature and concentration changes as the thermodynamic pressure is assumed to remain constant in open-boundary problems. In this work, the material derivative of density is related to the material derivatives of enthalpy and mass fraction of each species as

$$\frac{D\rho}{Dt} = \frac{\frac{\partial \rho}{\partial T} \Big|_{Y_i}}{\frac{\partial h}{\partial T} \Big|_{Y_i}} \frac{Dh}{Dt} + \sum_{i=1}^N \left(\frac{\partial \rho}{\partial Y_i} \Big|_{T, Y_{j \neq i}} - \frac{\frac{\partial \rho}{\partial T} \Big|_{Y_i}}{\frac{\partial h}{\partial T} \Big|_{Y_i}} \frac{\partial h}{\partial Y_i} \Big|_{T, Y_{j \neq i}} \right) \frac{DY_i}{Dt} \quad (30)$$

For a binary mixture, Eq. (30) is simplified to

$$\nabla \cdot \vec{u}^{n+1} = -\frac{1}{\rho^{n+1}} \frac{D\rho^{n+1}}{Dt} = \frac{1}{c_p \bar{v}} \frac{\partial \bar{v}}{\partial T} \Big|_{Y_i} \frac{Dh^{n+1}}{Dt} + \left(\frac{\rho}{W_1} \frac{\partial \bar{v}}{\partial X_1} \Big|_{T, X_{j \neq 1}} - \frac{\rho}{W_2} \frac{\partial \bar{v}}{\partial X_2} \Big|_{T, X_{j \neq 2}} - \frac{h_O - h_F}{c_p \bar{v}} \frac{\partial \bar{v}}{\partial T} \Big|_{Y_i} \right) \frac{DY_O^{n+1}}{Dt} \quad (31)$$

where \bar{v} is the mixture molar volume and W_1 and W_2 are the molecular weights of species 1 and species 2, respectively. All coefficients are evaluated at constant pressure and at time $n+1$, although it is not shown for the sake of a simpler notation. The thermodynamic partial derivatives that appear in Eq. (31) are obtained

using the thermodynamic model described in Section 3. Detailed expressions are available in Davis et al. [28].

Eq. (31) is only evaluated at single-phase cells once the interface location and the scalar fields have been updated in time. The material derivatives $\frac{Dh}{Dt}^{n+1}$ and $\frac{DY_o}{Dt}^{n+1}$ are computed using the RHS of the non-conservative governing equations, Eqs. (22) and (23), respectively.

At interface cells, a similar evaluation of $-\frac{1}{\rho} \frac{D\rho}{Dt}$ is not as straightforward as in the other cells, especially for the phase occupying less volume. Moreover, notice that each fluid compressibility can be associated to the divergence of phase-wise velocities (i.e., $\nabla \cdot \vec{u}_g = -\frac{1}{\rho_g} \frac{D\rho_g}{Dt}$ and $\nabla \cdot \vec{u}_l = -\frac{1}{\rho_l} \frac{D\rho_l}{Dt}$). Therefore, knowing the divergence of each phase-wise velocity in a narrow band of cells around the interface (including the interface cells) is necessary to determine the phase-wise velocities used in the VOF advection algorithm and in the governing equations, as well as the one-fluid velocity divergence from Eq. (40) used to solve the pressure-velocity coupling. To do so, the phase-wise velocity divergences are extrapolated from the real phase to a ghost region across the interface.

The multidimensional extrapolation techniques presented by Aslam [66] are used to populate this narrow band of cells with characteristic values of the compressibility of each fluid. For instance, Figure 4 shows the two-dimensional extrapolation region for liquid-based values. The extension to a three-dimensional configuration is straightforward and a similar definition is done to define the extrapolation region for gas-based values. Even though the details shown in [66] are based on an implementation of the extrapolation across regions defined by a LS function, the same methodology can be easily adapted to a VOF framework.

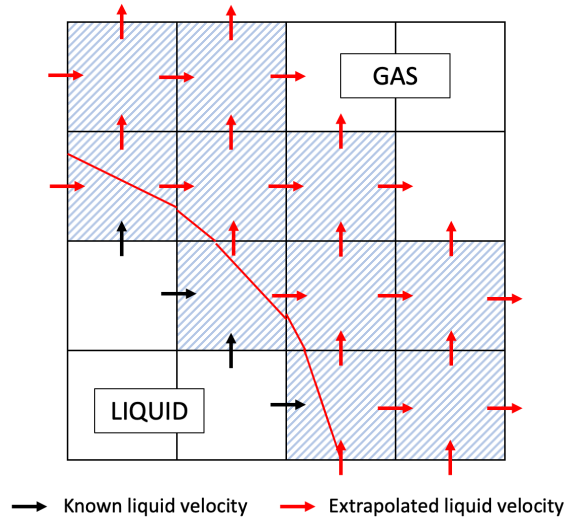


Figure 4: Definition of the extrapolation region (dashed cells) for liquid-phase values of fluid compressibility and phase-wise velocity in a two-dimensional mesh.

In the present code, a linear extrapolation of the divergence of each phase is performed. However, a constant extrapolation might be necessary for numerical stability depending on the problem configuration [57].

Using the extrapolation of the liquid-phase divergence as an example, Eqs. (32) and (33) have to be solved. The gas-phase divergence extrapolation follows the same approach.

$$\frac{\partial g_n}{\partial \tau} + H(C)(\vec{n} \cdot \nabla g_n) = 0 \quad (32)$$

$$\frac{\partial g}{\partial \tau} + H(C)(\vec{n} \cdot \nabla g - g_n) = 0 \quad (33)$$

In Eqs. (32) and (33), $g = \nabla \cdot \vec{u}_l$ and $g_n = \vec{n} \cdot \nabla g$. Here, \vec{n} is defined pointing towards the gas phase. These equations are solved to steady-state in a fictitious time τ , which does not necessarily have units of time. First, the normal gradient of g is extrapolated in a constant fashion using Eq. (32) and, then, g is extrapolated linearly following g_n using Eq. (33). The liquid-phase extrapolation is only performed in the region defined by $H(C)$, where $H(C) = 0$ if $C = 1$ and $H(C) = 1$ otherwise. That is, the extrapolation is done only at interface cells (i.e., $0 < C < 1$) and gas cells (i.e., $C = 0$). When extrapolating gas-phase values, $H(C) = 0$ if $C = 0$ and $H(C) = 1$ otherwise. For practical purposes, it is sufficient to reach steady-state only within the extrapolation region defined in Figure 4. If a constant extrapolation is required for numerical stability, it is necessary to solve Eq. (33) by setting $g_n = 0$. More information on the numerical discretization and solution of these two equations can be found in Aslam [66].

Within the VOF framework, the normal unit vector is defined only at interface cells. Therefore, we need to populate the extrapolation region with an estimate of \vec{n} in order to solve Eqs. (32) and (33). For that purpose, an inverse-distance weighted mean is used to average each component n_m (i.e., $m = x, y, z$) of \vec{n} at non-interface cells following Eq. (34). To evaluate this mean, only the information of the closest set of i interface cells in the neighborhood of the node of interest is used. d_i is defined as the distance between the node and the centroid of the interface plane in cell i . Once each mean n_m is obtained, the vector is re-normalized to have $|\vec{n}| = 1$.

$$n_m = \frac{\sum_i \frac{n_{m,i}}{d_i}}{\sum_i \frac{1}{d_i}} \quad (34)$$

Phase-wise velocities are obtained extending the extrapolation method discussed in Dodd et al. [42] to compressible flows. Eq. (35) is directly solved at steady-state conditions (i.e., as $\tau \rightarrow \infty$, $\frac{\partial \vec{u}_l}{\partial \tau} \rightarrow 0$) using an iterative solver until some desired tolerance is achieved. Like in Eqs. (32) and (33), here τ is a fictitious time-like variable that does not have units of time.

$$\frac{\partial \vec{u}_l}{\partial \tau} + \nabla(\nabla \cdot \vec{u}_l) = \nabla g \rightarrow \nabla(\nabla \cdot \vec{u}_l) = \nabla g \quad (35)$$

The two boundary conditions imposed in Eq. (35) are: a) the velocity components at the boundary of the extrapolation region inside the real phase are fixed and are equal to the one-fluid velocity. That is, $\vec{u}_l = \vec{u}$ in the example shown in Figure 4; and b) the velocity components at the boundary of the extrapolation region

in the ghost phase must satisfy the discrete divergence of the boundary cell (i.e., the extrapolated $\nabla \cdot \vec{u}_l$). The inner velocity components are solved by discretizing Eq. (35) using second-order finite differences. This methodology ensures that the extrapolated staggered phase-wise velocity field satisfies the extrapolated phase-wise divergence field. Although Eq. (35) only shows the extrapolation of liquid phase-wise velocities, the phase-wise velocities related to the gas phase are obtained using the same approach.

A note on the treatment of under-resolved regions must be done here. As pointed out in Sections 4.2 and 5.4, a minimum mesh resolution is needed to accurately capture the interface geometry and surface tension force for a time-marching solution of the governing equations. Moreover, the need to extrapolate phase-wise fluid compressibilities and velocities becomes problematic in under-resolved areas, where poor convergence (or none at all) of the extrapolation equations may arise.

A possible solution, but out of the scope of this work, would be to locally refine the mesh in these areas (i.e., use Adaptive Mesh Refinement or AMR). Here, a different approach is proposed. A group of nodes or “block” is defined around under-resolved interface locations. The nodes inside these under-resolved domains are excluded from both the phase-wise fluid compressibility and velocity extrapolations. In these areas, it is assumed that the extrapolation region is incompressible and the phase-wise velocities correspond to the one-fluid velocity. To maintain consistency with the pressure solver, $\nabla \cdot \vec{u}^{n+1} = 0$ at under-resolved interface cells as well. Phase change is still added during the advection of the volume fraction in these cells (i.e., Eq. (21a) is still used).

Under-resolved areas are identified in high-curvature regions where the local radius of curvature is below a certain resolution threshold. This threshold is defined as $1/\kappa < 3\Delta x$ in two dimensions, whereas in three-dimensions three curvatures and thresholds are considered: the three-dimensional curvature of the surface with $1/\kappa < 6\Delta x$ and the curvatures in the two principal directions used to determine the three-dimensional curvature with $1/\kappa_1 < 3\Delta x$ and $1/\kappa_2 < 3\Delta x$. That is, the three-dimensional curvature may be twice the curvature of a two-dimensional surface with the same radii of curvature (e.g., a circle and a sphere with the same diameter) and it may also be zero if the two radii of curvature cancel each other locally. Similarly, under-resolved areas are also defined around thin liquid structures or gas pockets where two conflicting extrapolations coming from two different interfaces exist.

The errors introduced with this treatment are expected to be minimal in regions where geometry errors already exist and might be dominant. The treatment of these under-resolved areas might also affect mass conservation since fluid compressibilities are neglected in the advection of the interface. The main goal here is to define a numerical approach that will keep the simulation advancing in time. For instance, the error introduced in the pressure solver when not accounting for the velocity jump due to mass exchange is related to the strength of \dot{m}' . For the type of flows analyzed here, the velocity jump $(\vec{u}_g - \vec{u}_l) \cdot \vec{n}$ may be of the order of $O(10^{-1} - 10^{-2} \text{ m/s})$ for a velocity field of the order of $O(10^1 \text{ m/s})$.

5.4. Discretization of the momentum equation and predictor-projection method

A one-fluid approach is used to solve the two-phase continuity and momentum equations in conservative form (i.e., Eqs. (1) and (2)). Following the work by Dodd and Ferrante [41], fluid properties are averaged on each cell by using the volume fraction occupied by each phase as $\phi = \phi_g + (\phi_l - \phi_g)C$, where ϕ is any fluid property such as density or viscosity. Thus, the one-fluid property is obtained from a volume average of each phase value, which diffuses the sharpness of the interface only within a region of $O(\Delta x)$. To satisfy the normal and tangential momentum jumps across the interface (i.e., Eqs. (7) and (8)), the effect of surface tension is added by means of a body force active only at the interface, $\vec{F}_\sigma = \vec{f}_\sigma \delta_\sigma(\vec{x} - \vec{x}_\Gamma)$.

The Continuum Surface Force (CSF) approach from Brackbill et al. [67] extended to flows with variable surface tension [68, 69] is used to replace $\vec{f}_\sigma = -\sigma\kappa\vec{n} + \nabla_s\sigma$ and the Dirac δ -function as $\delta_\sigma(\vec{x} - \vec{x}_\Gamma) = |\nabla C|$. The gradient of the surface tension coefficient tangent to the interface is evaluated using the method described in Seric et al. [69], which takes advantage of the HF technique (i.e., the same method used to evaluate interface curvature) to evaluate $\nabla_s\sigma = \frac{\partial\sigma}{\partial s_1}\vec{t}_1 + \frac{\partial\sigma}{\partial s_2}\vec{t}_2$ in a three-dimensional configuration. That is, the gradient at a given interface cell is directly evaluated along two orthogonal tangential directions, s_1 and s_2 . The reduction to a two-dimensional configuration is readily available. Similar to the evaluation of κ , a minimum resolution of the interface is needed to obtain accurate results [69].

Even though the MYC method is used to evaluate the interface normal unit vector, the approximation $\vec{n} = -\nabla C/|\nabla C|$ is taken in the modeling of the surface tension force in the momentum equation. This definition is also made when determining the tangential unit vectors at the interface. Therefore, the gradient of the volume fraction is used to provide directionality and locality to the surface tension force.

Finally, a density scaling is used to obtain a body force per unit volume which is independent of the fluid density [67, 68]. This modification generates a uniformly-distributed surface tension force which improves the performance of the CSF approach and reduces the magnitude of spurious currents at high density ratios.

Under all these considerations, the momentum equation is rewritten as

$$\frac{\partial}{\partial t}(\rho\vec{u}) + \nabla \cdot (\rho\vec{u}\vec{u}) = -\nabla p + \nabla \cdot \vec{\tau} + \frac{\rho}{\langle\rho\rangle} \left(\sigma\kappa\nabla C + \nabla_s\sigma|\nabla C| \right) \quad (36)$$

with $\langle\rho\rangle = \frac{1}{2}(\rho_G + \rho_L)$, where ρ_G and ρ_L are the initial pure gas and pure liquid densities, respectively. Similar to the normal force term $\sigma\kappa\nabla C$, the tangential force term $\nabla_s\sigma|\nabla C|$ is further simplified once the tangential unit vectors, \vec{t}_1 and \vec{t}_2 , are evaluated from the normal unit vector, \vec{n} .

The continuity-momentum coupling is addressed by using the predictor-projection method by Chorin [70]. The predictor step consists of a first-order, semi-explicit time integration of Eq. (36) without the pressure gradient, given by

$$\vec{u}^p = \frac{\rho^n \vec{u}^n}{\rho^{n+1}} + \frac{\Delta t}{\rho^{n+1}} \left[-\nabla \cdot (\rho\vec{u}\vec{u})^n + \nabla \cdot \vec{\tau}^n + \frac{\rho^{n+1}}{\langle\rho\rangle} \left(\sigma^{n+1}\kappa^{n+1}\nabla C^{n+1} + \nabla_s\sigma^{n+1}|\nabla C^{n+1}| \right) \right] \quad (37)$$

where the surface tension force term is evaluated implicitly. As shown in Figure 1, the interface location, the scalar fields and the interface equilibrium solution are updated before solving the Navier-Stokes equations. This way, the density at the new time, ρ^{n+1} , can be evaluated, as well as the interface curvature and surface tension coefficient, κ^{n+1} and σ^{n+1} . Since the advection of the interface is performed using first-order temporal accuracy (see Section 4), the temporal accuracy of \vec{u} and p is limited to first order as well [41]. Thus, higher-order temporal integrations in Eq. (37) (e.g., Adams-Bashforth scheme) might not add any major improvement to the flow solver.

After the predictor step, the projection step includes the pressure gradient term to correct \vec{u}^p in order to satisfy the continuity equation and provide \vec{u}^{n+1} as shown in Eq. (38).

$$\vec{u}^{n+1} = \vec{u}^p - \Delta t \frac{\nabla p^{n+1}}{\rho^{n+1}} \quad (38)$$

An equation for the pressure field is constructed by taking the divergence of Eq. (38) as

$$\nabla \cdot \left(\frac{\nabla p^{n+1}}{\rho^{n+1}} \right) = \frac{1}{\Delta t} \left(\nabla \cdot \vec{u}^p - \nabla \cdot \vec{u}^{n+1} \right) \quad (39)$$

where the resulting pressure field satisfies the continuity equation embedded in the term $\nabla \cdot \vec{u}^{n+1}$.

Following Duret et al. [44], $\nabla \cdot \vec{u}^{n+1}$ is evaluated by constructing a mass conservation equation for each phase. Substituting $\rho = \rho_g + (\rho_l - \rho_g)C = \rho_g(1 - C) + \rho_l C$ into Eq. (1), one gets, in the presence of phase change, the following relation

$$\nabla \cdot \vec{u}^{n+1} = -(1 - C) \frac{1}{\rho_g} \frac{D\rho_g}{Dt} - C \frac{1}{\rho_l} \frac{D\rho_l}{Dt} + \dot{m} \left(\frac{1}{\rho_g} - \frac{1}{\rho_l} \right) \quad (40)$$

Eq. (40) reduces to $-\frac{1}{\rho} \frac{D\rho}{Dt}$ away from the interface, which is the standard definition of the divergence of the velocity field in terms of density change of a fluid particle. At interface cells ($0 < C < 1$), the divergence of the one-fluid velocity field is obtained as the volume-averaged compressibilities of each phase plus the volume expansion (or compression) caused by the change of phase.

For low-Mach-number flows, the terms $\frac{1}{\rho_g} \frac{D\rho_g}{Dt}$ and $\frac{1}{\rho_l} \frac{D\rho_l}{Dt}$ are assumed to be independent of pressure. That is, density becomes a function only of thermodynamic pressure, temperature and composition. For open-boundary flows, the thermodynamic pressure remains constant. The evaluation of the fluid compressibilities has been discussed in Section 5.3.

Here, the split pressure-gradient method for two-phase flows proposed by Dodd and Ferrante [41] is used, where the substitution

$$\frac{1}{\rho^{n+1}} \nabla p^{n+1} \rightarrow \frac{1}{\rho_0} \nabla p^{n+1} + \left(\frac{1}{\rho^{n+1}} - \frac{1}{\rho_0} \right) \nabla \hat{p} \quad (41)$$

is made in Eqs. (38) and (39) with $\hat{p} = 2p^n - p^{n-1}$ being an explicit linear extrapolation in time of the pressure field and $\rho_0 = \min(\rho) \equiv \rho_G$. Notice that for the type of problems analyzed in this work, the lowest

density in the domain will always be the pure gas density, ρ_G . Thus, Eqs. (38) and (39) can be rewritten as

$$\vec{u}^{n+1} = \vec{u}^p - \Delta t \left[\frac{1}{\rho_0} \nabla p^{n+1} + \left(\frac{1}{\rho^{n+1}} - \frac{1}{\rho_0} \right) \nabla \hat{p} \right] \quad (42)$$

and

$$\nabla^2 p^{n+1} = \nabla \cdot \left[\left(1 - \frac{\rho_0}{\rho^{n+1}} \right) \nabla \hat{p} \right] + \frac{\rho_0}{\Delta t} (\nabla \cdot \vec{u}^p - \nabla \cdot \vec{u}^{n+1}) \quad (43)$$

Dodd and Ferrante [41] and Dodd et al. [42] validate the substitution from Eq. (41) with various benchmark tests. The substitution is exact when $\nabla \hat{p} \equiv \nabla p^{n+1}$ and approximate when $\nabla \hat{p} \approx \nabla p^{n+1}$. The accuracy of this method in predicting the pressure field is very good as long as the pressure is smooth in time (i.e., incompressible or low-Mach-number compressible flows). In two-phase flows, the pressure jump across the interface might become problematic in situations of combined high surface tension, curvature and density ratio (i.e., ρ_l/ρ_g), in which case the time step needs to be reduced to ensure sufficient temporal smoothness in \hat{p} and obtain a stable solution. For instance, the time step for the capillary wave at 10 bar shown in Section 6.2 had to be reduced considerably due to a higher density ratio than the other analyzed pressures (i.e., $\rho_l/\rho_g \approx 86$ at 10 bar vs. $\rho_l/\rho_g \approx 6.5$ at 150 bar).

The main advantage of the split pressure-gradient method is that Eq. (43) becomes a constant coefficient PPE under the low-Mach-number assumption (i.e., decoupled density and pressure). Combined with a uniform mesh, this equation can be solved using a fast Poisson solver based on performing a series of Discrete Fourier Transforms or FFT [41, 71]. This pressure solver can be adapted to various sets of boundary conditions [71] (e.g., periodic or homogeneous Neumann boundary conditions) and achieves computational speed-ups orders of magnitude larger than iterative solvers based on Gauss elimination (i.e., $O(10^2)$) or multi-grid solvers (i.e., $O(10)$). Furthermore, machine-error accuracy is obtained in the solution of the pressure field.

Since the momentum equation is presented in conservative form, Eqs. (37) and (43) are discretized in a staggered mesh using standard finite-volume techniques. Thus, velocity nodes are located at the center of the faces of the control volume defined around a pressure node. All fluid properties, as well as the volume fraction occupied by the liquid phase, are also defined at the pressure node.

The one-fluid approximation introduces some issues. The divergence of the viscous stress tensor, $\nabla \cdot \bar{\tau}$, is discretized with a second-order central-difference method using phase-wise velocities. If the one-fluid velocity were used in this term, an artificial pressure spike would exist across the interface due to the velocity jump in the presence of phase change, as discussed in [42]. To maintain numerical stability, accuracy and boundedness, the convective term, $\nabla \cdot (\rho \vec{u} \vec{u})^n$, is discretized using the SMART algorithm by Gaskell and Lau [72]. At interface cells, however, a hybrid method is used which alternates between the central differencing and upwind schemes depending on the cell Peclet number. Here, the one-fluid velocity must be used to capture the momentum jump caused by vaporization or condensation as seen in Eq. (7).

Regarding the volume averaging of fluid properties (i.e., density and viscosity), it only takes place at interface cells where $0 < C < 1$. In the compressible framework, the gas and liquid values of the interface solution are chosen as representative values for the averaging. Similarly, ρ_g and ρ_l appearing in the fluid expansion (or compression) term due to phase change in Eq. (40) are also obtained from the local interface solution, as well as the mass flux, \dot{m}' , used to evaluate \dot{m} .

Because velocity cells are staggered and interface properties are evaluated only at interface cells, there will not be always two adjacent interface cells which can be used to average the interface property (e.g., curvature). Any given interface property, ϕ , is averaged at the velocity node (i.e., cell face) as [41]

$$\phi_{i+1/2,j,k} = \begin{cases} \phi_{i+1,j,k} & \text{if } \phi_{i,j,k} = 0 \\ \phi_{i,j,k} & \text{if } \phi_{i+1,j,k} = 0 \\ \frac{1}{2}(\phi_{i+1,j,k} + \phi_{i,j,k}) & \text{otherwise} \end{cases} \quad (44)$$

Here, the location of a u -node is addressed and the same method can be used in all the other velocity nodes.

Eq. (44) is used to evaluate σ , κ , $\frac{\partial \sigma}{\partial s_1}$ and $\frac{\partial \sigma}{\partial s_2}$, which will only have a non-zero value at interface cells.

5.5. Time step criteria and final notes on the algorithm

The time step must satisfy the CFL condition for numerical stability in an explicit solver. A CFL condition similar to Kang et al. [73] is used here, which has been applied successfully in other works [44, 74].

The following conditions are defined to determine the time step magnitude, Δt :

$$\begin{cases} \tau_{\vec{u}} = \frac{|u|_{\max}}{\Delta x} + \frac{|v|_{\max}}{\Delta y} + \frac{|w|_{\max}}{\Delta z} \\ \tau_{\mu} = \left(\frac{2}{\Delta x^2} + \frac{2}{\Delta y^2} + \frac{2}{\Delta z^2} \right) \left(\frac{\mu}{\rho} \right)_{\max} \\ \tau_{\sigma} = \sqrt{\frac{\sigma_{\max} \kappa_{\max}}{\rho_{\min} \min(\Delta x^2, \Delta y^2, \Delta z^2)}} \end{cases} \quad (45)$$

$$\Delta t_{\vec{u}} = \frac{2}{\tau_{\vec{u}} + \tau_{\mu} + \sqrt{(\tau_{\vec{u}} + \tau_{\mu})^2 + 4\tau_{\sigma}^2}} \quad (46)$$

$$\Delta t_h = \frac{\min(\Delta x^2, \Delta y^2, \Delta z^2)}{2\alpha_{\max}} \quad (47)$$

$$\Delta t_Y = \frac{\min(\Delta x^2, \Delta y^2, \Delta z^2)}{2(D_m)_{\max}} \quad (48)$$

$$\Delta t = C_{\text{CFL}} \min(\Delta t_{\vec{u}}, \Delta t_h, \Delta t_Y) \quad (49)$$

where $\alpha = \lambda/(\rho c_p)$ and $C_{\text{CFL}} = 0.1 - 0.2$ is chosen conservatively low. The choice of C_{CFL} is a numerical compromise between numerical stability and computational cost.

The computational cost of this algorithm is larger than similar algorithms for incompressible flows without phase change. Usually, the main cost of any fluid dynamics simulation is linked to the pressure solver. However, the split pressure-gradient method is very efficient and useful for incompressible and low-Mach-number configurations. Three major necessary steps are responsible for at least 40% of the computational cost per time step: the solution of LTE at all interface cells, the update of fluid properties using the thermodynamic model and the extrapolation of phase-wise fluid compressibilities and velocities.

Moreover, there is a scalability issue for problems where the interface deforms considerably, such as those aiming to study liquid jet injection. As the interface grows and deforms, more interface nodes are added and the thermodynamic and topology complexity of the interface increases. Moreover, the convergence rate of phase-wise extrapolations might be reduced. Thus, the computational cost per time step may increase over time.

6. Results

The results presented in this work cover the relevant characteristics seen in supercritical liquid injection environments. Since no analytical solutions are available at these conditions and the chosen thermodynamic model influences the final results, the focus here is on the qualitative correctness of the observed physics. Similar codes have been widely tested and validated in simpler scenarios (e.g., incompressible flow with or without phase change [40–42, 57]). Thus, the validation of the present code in these cases is not shown here.

The one-dimensional results presented in Section 6.1 have been obtained with a linear extrapolation of the velocity divergence of each phase. To ensure a stable solution, the results presented in Sections 6.2, 6.3 and 6.4 perform a constant extrapolation of the velocity divergence.

6.1. One-dimensional unsteady flow near the liquid-gas interface

The transient behavior around a liquid-gas interface with zero curvature at various pressures has been analyzed using a two-dimensional configuration with an initially straight interface and no shear flow. A more complete analysis of this problem is presented in Poblador-Ibanez and Sirignano [13], where a one-dimensional code is used to analyze this problem. The main differences between both approaches are that here the interface is allowed to move as mass exchange and volume expansion occur and the full set of governing equations are solved, whereas in [13] the solution is obtained relative to the interface by fixing its location and pressure is assumed to be constant throughout the entire domain. Thus, the momentum equation is not solved in [13] and the velocity field is directly obtained from the continuity equation.

The problem configuration consists of a liquid *n*-decane at $T_L = 450$ K sitting on a wall surrounded by a hotter gas (i.e., pure oxygen) at $T_G = 550$ K. With both fluids initially at rest, the liquid-gas interface will reach a state of thermodynamic equilibrium as oxygen dissolves into the liquid and *n*-decane vaporizes. The initial interface location is $50\ \mu\text{m}$ away from the wall. Volume expansion/compression due to the

mixing process and phase change generate a velocity field perpendicular to the interface. Periodic boundary conditions are imposed in the y -direction, while no-slip wall boundary conditions are imposed at $x = 0$ and an open-boundary is imposed sufficiently far away from the interface in the gas phase. Since there is no interface perturbation (except for small numerical errors due to machine precision) or shear flow, the two-dimensional code must predict a one-dimensional solution. Four different pressures are analyzed: one subcritical case at 10 bar and three supercritical cases with 50, 100 and 150 bar [13]. A mesh size of $\Delta x = 200$ nm and time step of $\Delta t = 2$ ns are used for all pressures.

A direct comparison between the results from the present work and the results shown in Poblador-Ibanez and Sirignano [13] is not possible because the thermodynamic models used in both works are not exactly the same. Here, a volume correction is implemented to enhance the accuracy of the SRK equation of state, whereas in [13] this correction is not added. Thus, different fluid properties are predicted, especially in the liquid phase. Nevertheless, a qualitative comparison is possible.

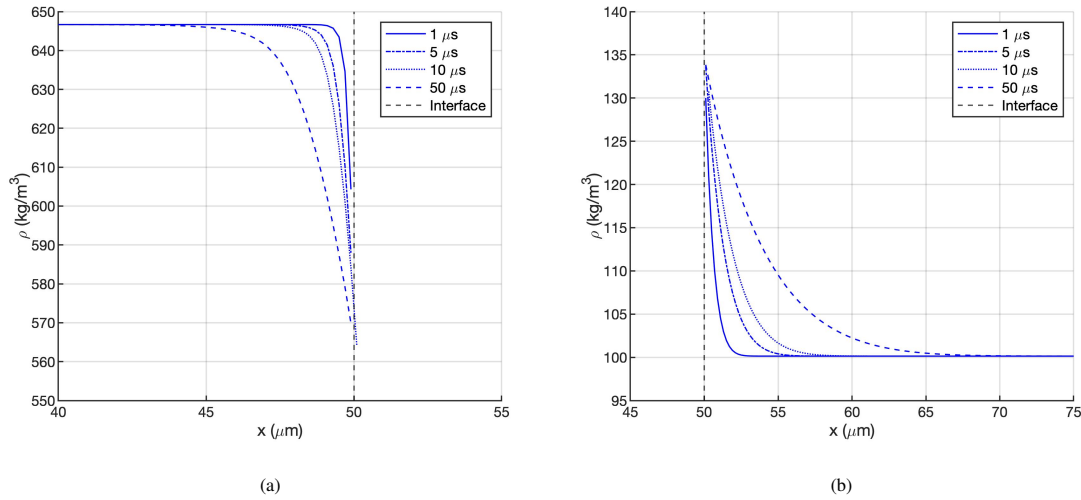


Figure 5: Temporal evolution of the density profiles for the one-dimensional unsteady flow near a liquid-gas interface for an oxygen/n-decane binary mixture at $p = 150$ bar. (a) liquid density; (b) gas density.

The results are definitely one-dimensional. No indication of a deviation or instability is found. Figure 5 shows the temporal evolution of density profiles at 150 bar. Overall, the results look very similar to those shown in [13] except for minor differences caused by the improvement in the thermodynamic model. For instance, the predicted liquid density (Figure 5a) is larger than the one shown in [13], but it is also more accurate when compared to reference data from NIST. The denser liquid causes thermal and mass diffusion to occur slightly slower than in [13]. Mixing in the gas phase is very similar in both works, where the density profile extends about 7-9 μm into the gas phase at $t = 10 \mu\text{s}$ and the temperature profile extends about 10 μm in the same amount of time. As the mixing layers grow in time, the interface tends to a steady-state solution as reported in [13] (see Figure 6b). Similar works dealing with a two-dimensional laminar mixing layer

show the same trend [28, 29]. Nevertheless, this behavior may not be true in more complex flows where the interface deforms.

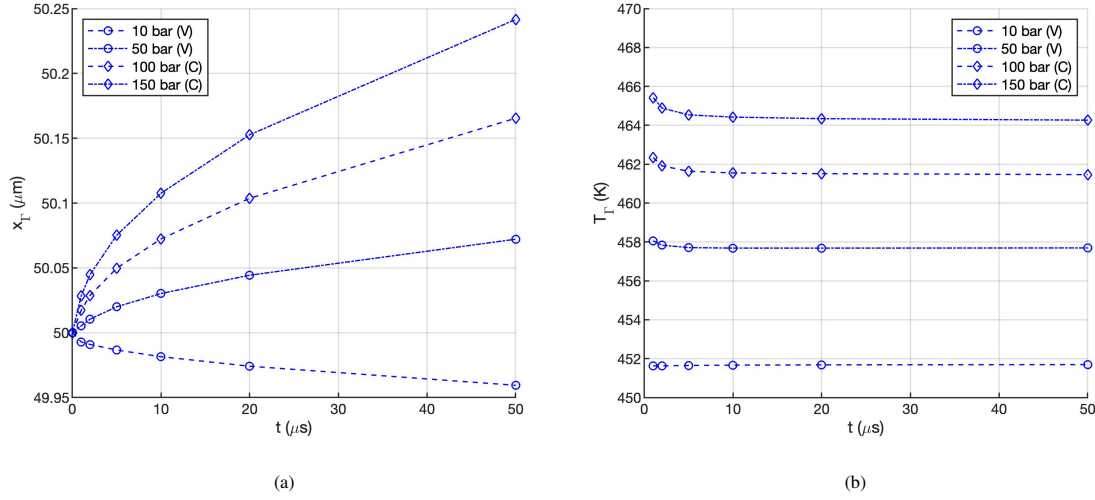


Figure 6: Temporal evolution of the interface location and temperature at different pressures for the one-dimensional unsteady flow near a liquid-gas interface for an oxygen/*n*-decane binary mixture. Depending on the ambient pressure, net vaporization (V) or net condensation (C) occurs across the interface. (a) interface location; (b) interface temperature.

Lastly, the two main assumptions done in [13] are justified here. Throughout the simulation, pressure remains nearly constant and the velocity field is mainly driven by density changes caused by mixing. Moreover, Figure 6a shows the interface location as time marches. Because under this problem configuration mass exchange weakens as mixing occurs, the interface displacement is actually negligible. The maximum interface displacements after $50 \mu\text{s}$ are of the order of 100 nm, which are similar to the Δx used in the mesh of this problem and negligible compared to the thickness of the diffusion layers.

The direction of the interface displacement discussed in [13] is also confirmed. At 10 bar, net vaporization is strong with very little dissolution of oxygen into the liquid phase. Thus, the interface recedes and the overall liquid volume decreases. However, as pressure increases, the dissolution of oxygen into *n*-decane is enhanced. Therefore, the lighter species causes local liquid volume expansion near the interface. At 50 bar, even though the interface presents net vaporization, it is not strong enough to compensate for the liquid volume expansion. At 100 bar and 150 bar, both local volume expansion and net condensation contribute to the overall increase in liquid volume. This feature of high-pressure, two-phase flows may cause the interface to simultaneously present net condensation and net vaporization at different locations depending on its deformation and the heat flux into the interface [15].

6.2. Two-dimensional standing wave at supercritical pressures

The standing wave problem is an appropriate test to validate the relaxation time of a perturbed two-phase interface driven by capillary forces. Gravity is neglected here, although the analytical solution of this problem for incompressible flows with infinite depth proposed by Prosperetti [75] may include it. Dodd and Ferrante [41] validate their two-phase code for incompressible flows without phase change and analyze the capillary wave problem with evaporation to verify the spatial convergence of their two-phase code [42].

Here, a similar analysis is performed for the same binary mixture of oxygen and *n*-decane seen in Section 6.1. Each phase has the same initial temperature and composition, but the analyzed thermodynamic pressures vary between 10, 50, 100 and 150 bar. The two-dimensional domain is a rectangular box of 30 μm wide with a liquid layer of 20 μm depth. The liquid-gas interface is spatially perturbed with a sinusoidal wave of 1 μm amplitude and 30 μm wavelength, while both fluids are initially at rest. The amplitude-to-wavelength ratio of 1/30 can be considered a small interface perturbation. The height of the domain must englobe the mixing region in both phases during the analyzed times. For 100 and 150 bar, a height of 60 μm is enough. For 50 bar, it is changed to 70 μm and, for 10 bar, to 100 μm . Periodic boundary conditions are imposed in the *x*-direction (i.e., tangential to the interface), open-boundary (i.e., outflow) conditions are imposed in the *y*-direction at the end of the gas-phase domain and no-slip wall boundary conditions are imposed at the bottom of the liquid layer.

The mixing in both phases is very similar to the one-dimensional case since the interface perturbation is small and there is no shear flow. The relaxation of the interface deformation caused by capillary forces drives the overall picture further towards a one-dimensional solution. Nevertheless, this transient process allows us to study the accuracy and resolution of the numerical model.

6.2.1. Spatial convergence

The 150 bar case is chosen to analyze the spatial convergence of the numerical model under interface deformation. The temporal convergence is expected to be first order because of how the equations are discretized. Thus, it is not analyzed here and we rely on a sufficiently small CFL condition to minimize temporal errors. Table 1 presents the four different uniform meshes that are studied and Figures 7, 8, 9 and 10 show results of the interface geometry and equilibrium solution at 19 μs .

Mesh	M1	M2	M3	M4
Δx (μm)	3/10	2/10	1/10	1/20
Cells/Wavelength	100	150	300	600
Cells/Amplitude	3.33	5	10	20

Table 1: Mesh properties used in the analysis of a two-dimensional capillary wave at supercritical pressures. The number of cells per wavelength or amplitude refer to the initial configuration of the liquid-gas interface.

The matching solution along the interface is sensitive to the mesh resolution around it. Although many interface properties can be used, here the profiles of temperature, net mass flux and oxygen mass fraction on both sides of the interface are shown (see Figures 7 and 8). As the mesh is refined, the mixing around the interface is captured better and the enthalpy and concentration gradients obtained using the normal probe technique (Section 5.2) become more accurate. Moreover, the PLIC interface reconstruction tends to a more continuous interface shape. This translates into a smoother distribution of fluid properties along the interface as seen in Figures 7, 8 and 10a.

The apparent deviation between two consecutive meshes is only enlarged by the scale of the figures. Although M1 (i.e., $\Delta x = 0.3 \mu\text{m}$) might look like an outlier due to a poorer resolution, especially of the liquid phase mixing region, the normalized errors or differences in the solution between two consecutive meshes are of the order of 1% or less. A thorough analysis shows the normalized errors converge with a first-order rate or lower, which is expected given the complexity of the numerical approach. Other works with simpler models to determine the interface properties also report similar issues [42, 57]. Even though one-dimensional interfaces show good grid independence, limited spatial convergence appears once two-dimensional or three-dimensional interfaces are analyzed.

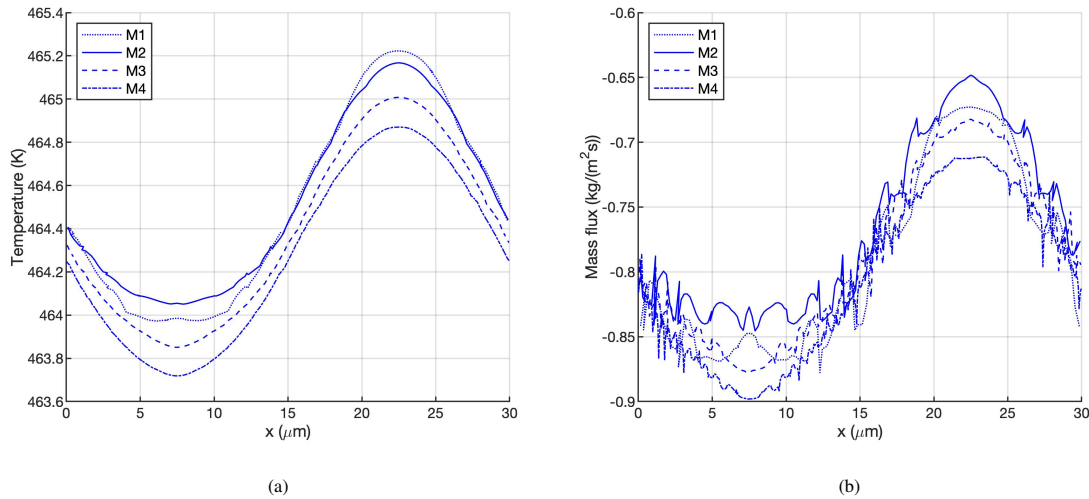


Figure 7: Interface geometry and matching solution of the two-dimensional capillary wave at $t = 19 \mu\text{s}$ for the 150 bar case. (a) temperature; (b) net mass flux.

Although the matching solution along the interface looks smooth as the mesh is refined, the net mass flux across the interface, \dot{m}' , is not (see Figure 7b). As explained in [29], \dot{m}' is very sensitive to small changes in equilibrium composition or temperature. Thus, imperceptible perturbations are captured in \dot{m}' . Moreover, the normal probe used to determine the LTE and jump conditions is actually built on the PLIC interface. It is not guaranteed that the PLIC interface will be continuous across cells and, furthermore, it loses any information on local interface curvature (i.e., the interface is represented by a plane). Therefore, the nature

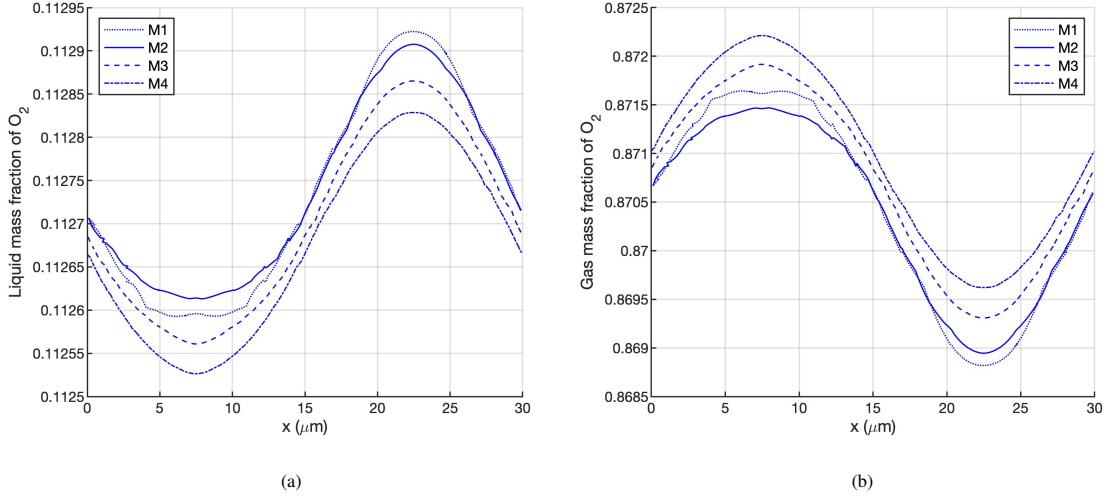


Figure 8: Interface geometry and matching solution of the two-dimensional capillary wave at $t = 19 \mu s$ for the 150 bar case. (a) oxygen mass fraction in the liquid phase; (b) oxygen mass fraction in the gas phase.

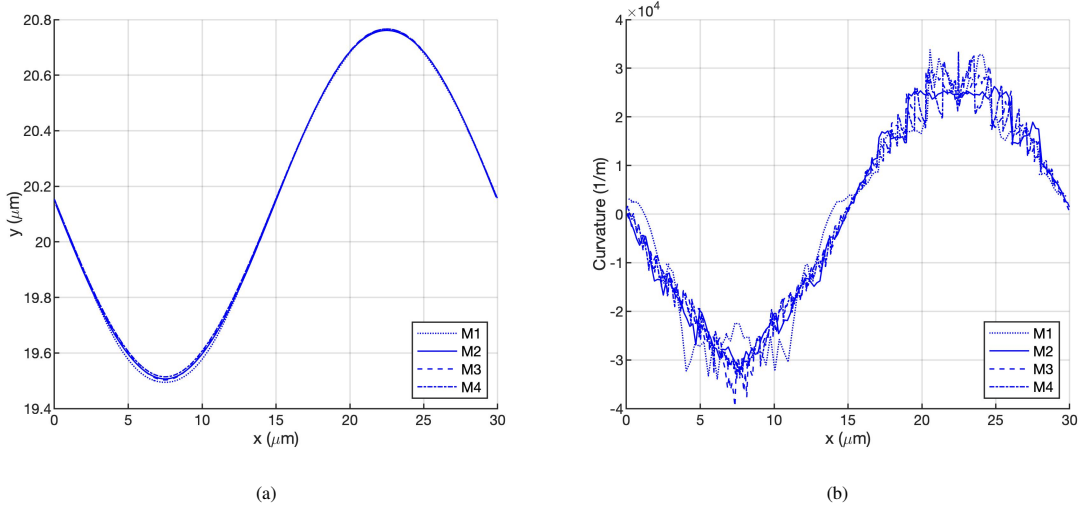


Figure 9: Interface geometry and matching solution of the two-dimensional capillary wave at $t = 19 \mu s$ for the 150 bar case. (a) interface amplitude; (b) curvature.

of the construction of the normal probes is in line with the observed disturbances.

Similar oscillations appear when evaluating the curvature and the gradient of the surface tension coefficient (Figures 9b and 10b). Even though the interface shape and the distribution of the surface tension coefficient look smooth (Figures 9a and 10a), κ and $\nabla_s \sigma$ are evaluated using the HF method. This method is known to present these perturbations albeit converging with mesh refinement, as discussed in Section 4.2. Moreover, VOF methods using a one-fluid approach to solve the momentum equation will also present some degree of oscillations in the velocity and pressure fields near the interface due to the sharp averaging of fluid

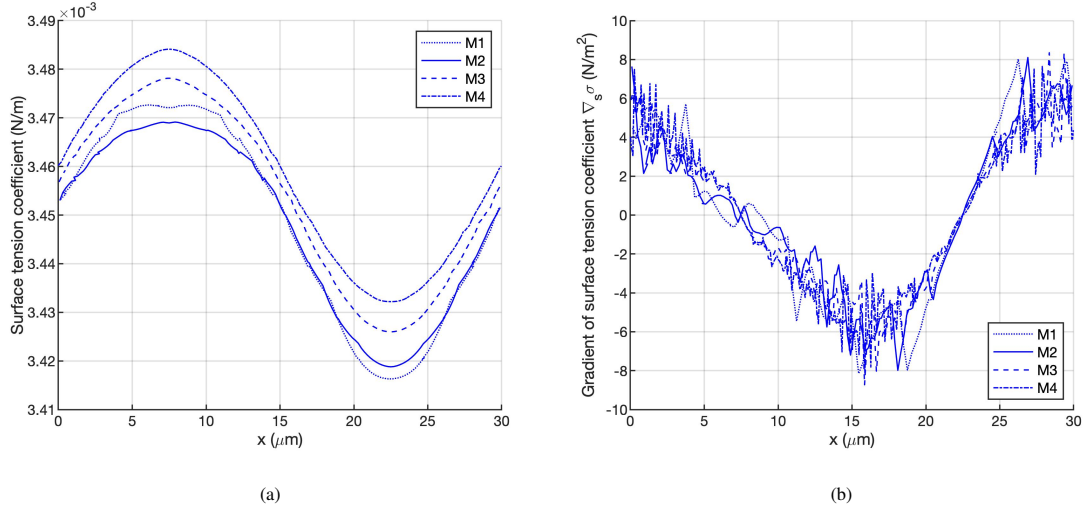


Figure 10: Interface geometry and matching solution of the two-dimensional capillary wave at $t = 19 \mu\text{s}$ for the 150 bar case. (a) surface tension coefficient; (b) surface tension coefficient gradient.

properties.

As seen in Figures 9a and 11, the slow spatial convergence of the interface matching solution and the small oscillations in some of the parameters have little effect on the relaxation of the interface amplitude. Figure 11a shows the temporal evolution of the vertical position of the interface at $x = 7.5 \mu\text{m}$, which corresponds to the initial location of the wave crest, and Figure 11b represents the interface vertical position at the initial location of the wave trough at $x = 22.5 \mu\text{m}$. Figures 9a and 11 verify the grid convergence of the numerical modeling with regards to the interface displacement.

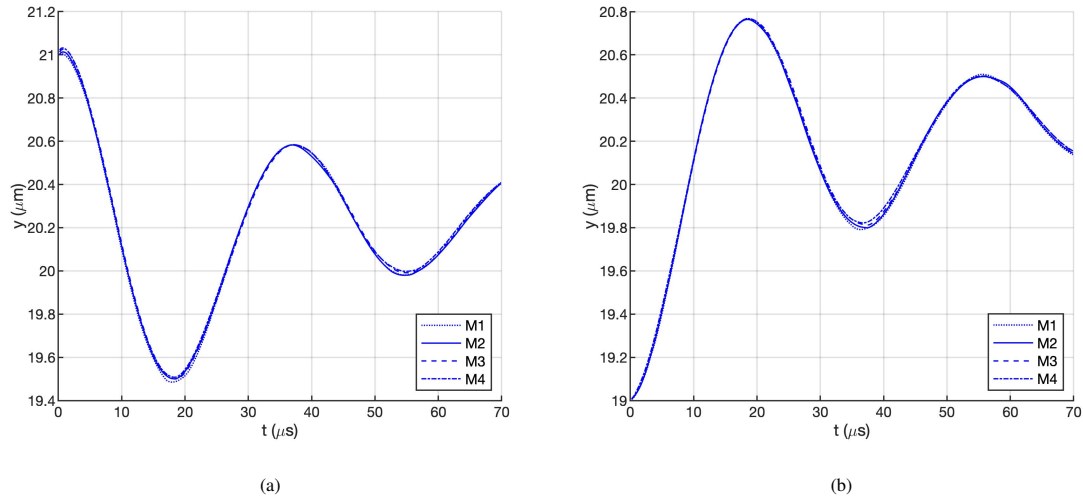


Figure 11: Interface amplitude relaxation of the two-dimensional capillary wave at 150 bar. (a) at $x = 7.5 \mu\text{m}$ (initial wave crest location); (b) at $x = 22.5 \mu\text{m}$ (initial wave trough location).

The total change in liquid volume and mass is shown in Figure 12. A convergent trend with mesh refinement is observed, especially in the total liquid volume (see Figure 12a). The strong condensation during the initial stages of the problem is well captured with both meshes M3 and M4. However, differences in the mass flux and the accuracy to which density variations are captured cause the curves to deviate as time marches. Overall, a similar scenario as discussed for the interface properties is apparent here. Grid convergence is likely, but with a first-order rate or lower.

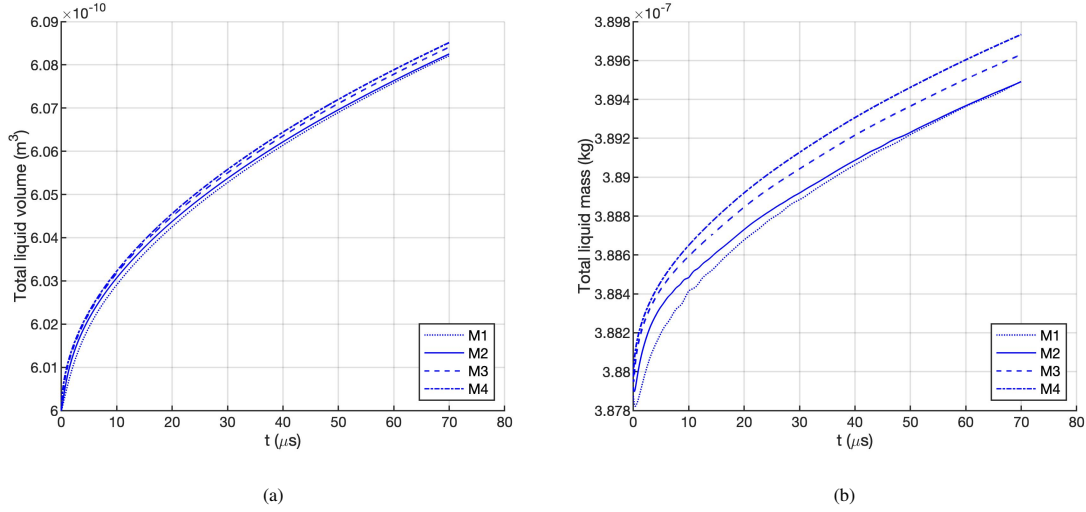


Figure 12: Temporal evolution of the total liquid volume and the total liquid mass for the two-dimensional capillary wave at 150 bar. (a) total liquid volume; (b) total liquid mass.

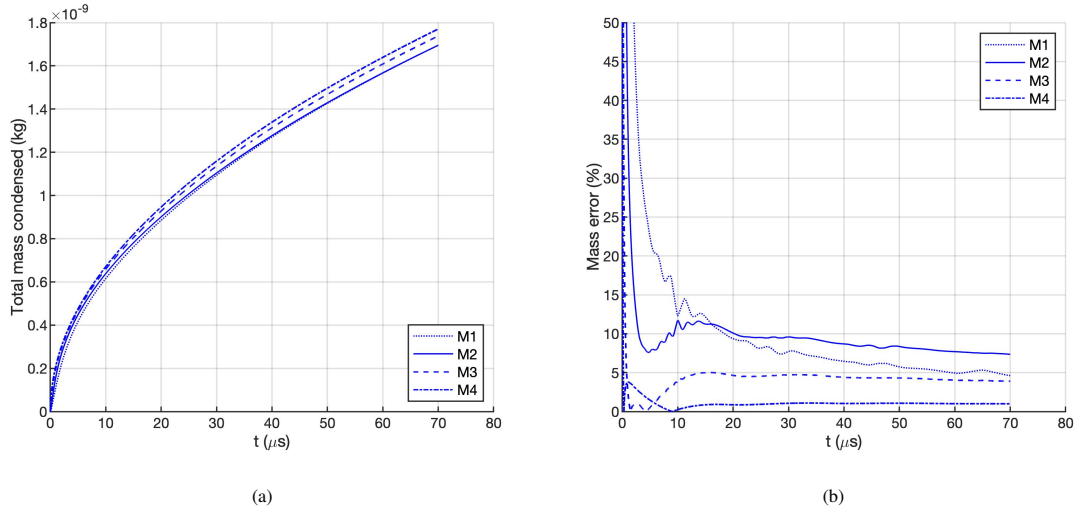


Figure 13: Temporal evolution of the total net mass exchanged across the interface and the estimated mass error for the two-dimensional capillary wave at 150 bar. (a) total mass condensed; (b) mass error.

Looking more closely at mass errors in the liquid phase, the total amount of mass that condenses at the interface (see Figure 13a) also converges with mesh refinement and should be equal to the difference between the total liquid mass at a given time and the initial liquid mass. Here, the total liquid mass is estimated at every time step as $m_L = \sum_{i,j,k} \rho_{i,j,k} C_{i,j,k} \Delta x \Delta y \Delta z$, with $\rho_{i,j,k}$ being the interface liquid density in interface cells. On the other hand, the total condensed mass is obtained as $m_{\text{cond}} = - \sum_{t_{\text{initial}}}^{t_{\text{final}}} \sum_{i,j,k} \dot{m}' A_{\Gamma} \Delta t$. Recall \dot{m}' is only non-zero at interface cells and A_{Γ} represents the area of the local interface plane at a given cell.

Even though both approaches should be equivalent, they manifest the mesh resolution issues with capturing both the density field and solving the jump conditions and LTE at the interface. Nevertheless, Figure 13b shows that the mass error evaluated as $E_m(\%) = 100(m_L - m_{\text{initial}} - m_{\text{cond}})/m_{\text{cond}}$ is reduced with mesh refinement and after some temporal development of the mixing regions. Although errors exist and mass conservation depends on mesh resolution, the overall thermodynamics of the interface can still be captured (e.g., identify regions of high or low mass exchange rate, whether condensation or vaporization occurs). These errors are expected to be larger in liquid injection problems as interface deformation generates smaller liquid structures. Thus, a fixed mesh resolution may lose accuracy in capturing both density variations and a smooth interface solution. Nevertheless, the total mass exchanged across the interface only represents between 0.1-1% of the total liquid mass in the amount of time analyzed in this work. Therefore, mass errors as defined by E_m become negligible when compared to the total liquid mass m_L .

The results presented in this section highlight the complexity of the numerical modeling for two-phase supercritical flows, but at the same time verify the consistency of the methodology implemented in this work. Searching for efficient and reliable methods translates into limited grid convergence rate for many parameters of the interface and global solution. Therefore, the mesh used in atomization simulations must be a compromise between computational cost and interface accuracy (i.e., geometry and solution of LTE and jump conditions).

6.2.2. Pressure effects

The two-dimensional capillary wave has been analyzed for the same four pressures used in Section 6.1 (i.e., 10, 50, 100 and 150 bar) with the uniform mesh M3 with $\Delta x = 0.1 \mu\text{m}$. The initial conditions used for all pressures are identical to those previously discussed. The goal here is to present the main differences in the interface thermodynamics as pressure transitions from subcritical to supercritical values.

The total volume change of the liquid phase with time is very similar to the one-dimensional problem (see Figure 14a). At 50, 100 and 150 bar the liquid phase expands near the interface and, together with condensation in the 100 and 150 bar cases, the total liquid volume increases with time. On the other hand, at 10 bar vaporization drives the reduction of the volume of the liquid phase. When analyzing the total liquid mass change over time presented in Figure 14b, the thermodynamic transition whereby net vaporization turns into net condensation as pressure increases is observed.

The deformation of the interface in the capillary wave test already shows some of the features of the interface thermodynamic behavior at high pressures. As seen in Figure 15, the effects of compressed mixing layers can cause the interface to simultaneously vaporize and condense in different locations. As noted in [15], regions of compressed (heated) gas may present a stronger vaporization or weaker condensation, whereas regions of compressed liquid show weaker vaporization or stronger condensation, depending on the ambient pressure. In limiting cases where mass exchange across the interface is already weak, such as at 50 bar, small interface deformations already cause this reversal.

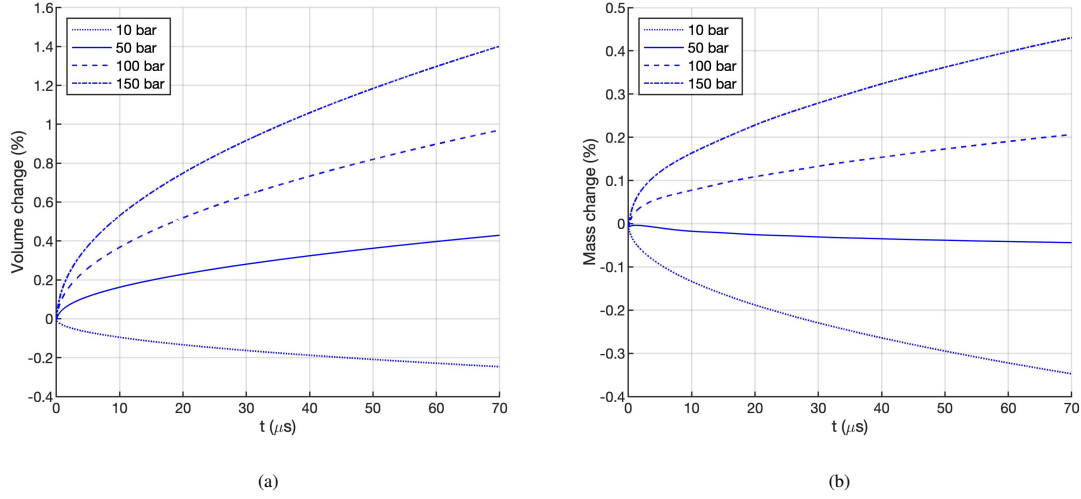


Figure 14: Temporal evolution of the liquid volume and the liquid mass for the two-dimensional capillary wave at 10, 50, 100 and 150 bar using mesh M3. (a) liquid volume change; (b) liquid mass change.

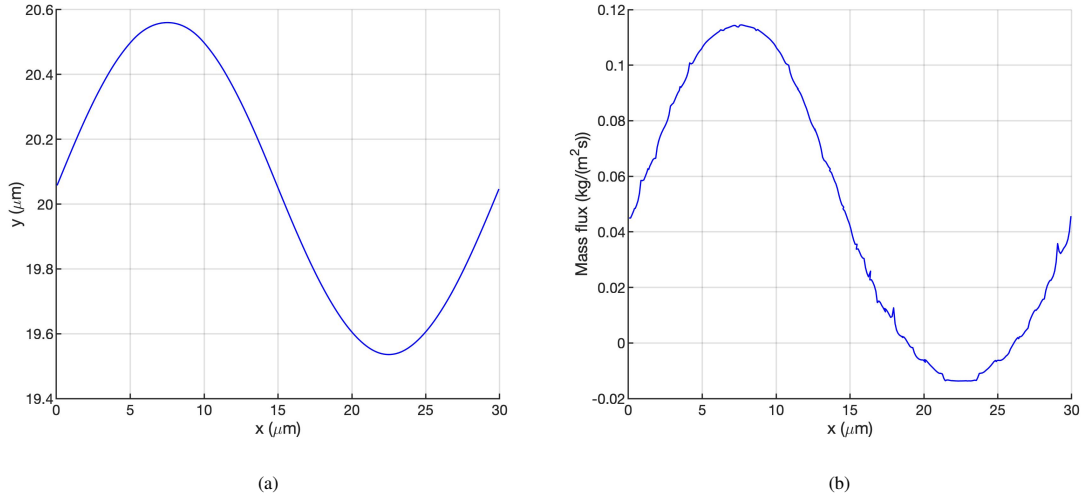


Figure 15: Interface geometry and matching solution of the two-dimensional capillary wave at $t = 24.94 \mu\text{s}$ for the 50 bar case using mesh M3. (a) interface amplitude; (b) net mass flux.

Another important feature of high-pressure two-phase flows is the reduction of surface tension forces with subsequent increase in the time for dynamic relaxation to smaller surface area. Figure 16 shows the relaxation of the wave amplitude over time at different pressures. The vertical position of the interface at the initial wave crest location of $x = 7.5 \mu\text{m}$ is shown in Figure 16a and the interface vertical location at the initial wave trough location of $x = 22.5 \mu\text{m}$ is shown in Figure 16b. It is important to notice a stronger reaction to the sharp initial conditions at 10 bar, where the interface displacement deviates considerably from the behavior at higher pressures. Nevertheless, clear conclusions can be extracted.

The effect of volume expansion is noticed as the wave amplitude presents a drift to higher y values as pressure increases. Moreover, higher surface tension forces at lower pressures cause higher-frequency interface oscillations. Even though the liquid viscosity near the interface drops as pressure increases due to enhanced mixing, the coupled dynamic system produces similar wave amplitude damping for all analyzed pressures. Reference values of surface tension coefficient and interface liquid and gas densities and viscosities are available in Davis et al. [28]. In there, the same thermodynamic model used here is implemented but no interface deformation exists. Still, the small deformations of the capillary wave test do not change significantly the interface solution.

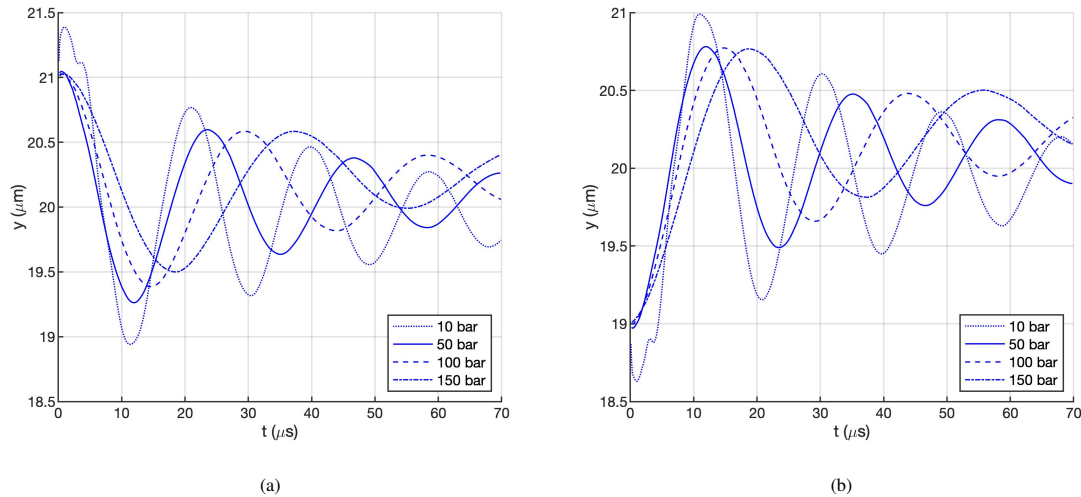


Figure 16: Interface amplitude relaxation of the two-dimensional capillary wave at 10, 50, 100 and 150 bar using mesh M3. (a) at $x = 7.5 \mu\text{m}$ (initial wave crest location); (b) at $x = 22.5 \mu\text{m}$ (initial wave trough location).

6.3. Two-dimensional planar jet at supercritical pressures

A temporal study of a symmetric two-dimensional planar jet is performed to demonstrate the ability of the numerical model in capturing the interface deformation and the relevant high-pressure physics during liquid injection. Although planar jets might develop an antisymmetric behavior [23], the computational cost conditions the problem configuration for these tests of the computational method.

The jet half-thickness is $H = 10 \mu\text{m}$ and the interface is initially perturbed with a sinusoidal wave of $30 \mu\text{m}$ wavelength and $0.5 \mu\text{m}$ amplitude. A thin velocity distribution is imposed around the interface, where the streamwise velocity varies from 0 in the liquid phase to 30 m/s in the gas phase with a hyperbolic tangent profile. Periodic boundary conditions are imposed in the streamwise direction and outflow boundary conditions are imposed in the gas phase away from the interface. The thermodynamic pressure is 150 bar and the initial conditions of each phase are the same as in the previous problems: the liquid jet is initially composed of pure *n*-decane at 450 K and the surrounding gas is pure oxygen at 550 K. Only one wavelength is enclosed in the computational domain and periodicity in the streamwise direction is used when plotting the results.

The low-Mach number domain is verified using the thermodynamic model. At this high pressure, the speed of sound in the gas phase is approximately 450 m/s. Therefore, a gas velocity of 30 m/s results in a Mach number of $M \approx 0.0667$. Actually, the development of a compressible pressure equation (not the PPE presented in this work) shows that compressible terms related to temporal variations in the pressure field (i.e., wave-like equation) scale with $M^2 \approx 0.00444 \sim O(10^{-3})$, which can be reasonably neglected. Faster jet velocities up to 100 m/s could be analyzed in future works with $M^2 \sim O(10^{-2})$ as a limit before the low-Mach-number model needs to be revised.

6.3.1. Mesh resolution and mass conservation

The results presented in Section 6.2 show good mesh convergence and mass-conservation properties for configurations with small deformations. In other words, situations where the mesh can resolve the shape of the liquid with high accuracy. However, liquid atomization problems present a cascade process whereby smaller and more complex liquid structures develop before they break up into droplets.

For a uniform mesh, the evolution of the liquid surface presents some degree of mesh dependence once under-resolved areas exist (e.g., high curvature regions). Not only the geometrical properties that define the interface are less accurate, but also the complex methodology presented in this work is affected as discussed previously (e.g., extrapolations of phase-wise values). Some solutions to this problem exist, like using local mesh refinement near these under-resolved regions. However, they are not pursued here to avoid increased modeling complexity. Because the mesh cannot be refined indefinitely for computational and physical constraints, an analysis of mesh dependence both in the liquid surface deformation and mass conservation properties is presented in this section. Three different uniform mesh sizes between M3 and M4 (see Table 1) are analyzed. Their characteristics are presented in Table 2.

Figures 17, 18 and 19 show the evolution of the temperature field and the interface deformation obtained with each mesh J1, J2 and J3. For the early times (i.e., $t \leq 4.5 \mu\text{s}$), detailed close-ups of the interface perturbation are shown. A broader picture is presented once the liquid deformation becomes more chaotic. The three meshes show almost an identical evolution up to $t \approx 1.5 \mu\text{s}$. Then, the coarser mesh J1 starts to

Mesh	J1	J2	J3
Δx (μm)	1/10	1/15	1/20
Cells/Wavelength	300	450	600
Cells/Amplitude	5	7.5	10

Table 2: Mesh properties used in the analysis of a two-dimensional planar liquid jet at supercritical pressures. The number of cells per wavelength or amplitude refer to the initial configuration of the liquid-gas interface.

deviate from J2 and J3. Deviations between J2 and J3 start to appear after $2.5 \mu\text{s}$.

Overall, the qualitative evolution of the interface is very similar in J1, J2 and J3, even for longer times. Deviations are observable once small liquid structures (with respect to the mesh size) develop. As mentioned during the paper, these poorly-resolved regions will suffer from less accurate interface geometrical and thermodynamic properties, as well as some simplifications to the numerical methodology have to be implemented to allow for extensive temporal development. Therefore, the liquid surface is prone to evolving differently once these mesh constraints appear.

Another important consideration relates to the varying fluid properties at these high pressures. Compared to grid-independence studies in two-phase incompressible flows, the resolution with which, for instance, the variable-density field is captured here also has an impact in the dynamics of the liquid phase. Thus, many more factors contribute to the mesh performance.

A mass conservation analysis is also performed for the liquid jet. Mass errors are evaluated as defined in Section 6.2.1. A worse performance than the standing wave problem is observed. The generation of smaller liquid structures typical of atomization problems is problematic for fixed meshes, not only in determining the evolution of the liquid surface, but also when satisfying mass conservation.

J1 is the worst performing mesh, with considerable deviations from J2 and J3 early in the simulations. J2 and J3 present a similar performance until the liquid evolution starts to differ (see Figures 20 and 21). Total liquid volume remains nearly similar up to $6 \mu\text{s}$, however deviations in total liquid mass and total net mass condensed across the interface appear much sooner ($t \approx 3 - 4 \mu\text{s}$). Mass errors are below 50% up to $2 \mu\text{s}$ and then they increase indefinitely as the deformation cascade process occurs. These mass errors are still fairly negligible if compared to the total liquid mass.

It is important to notice that these errors are mainly related to a worse resolution of the liquid density and the interface, but not to the ability of the model to predict condensation and vaporization rates with reasonable accuracy, even for small liquid structures. As seen in Figures 20 and 21, the overall mass exchange across the interface clearly results in net condensation up to $6 \mu\text{s}$, with the liquid shape still being well-defined with none or minimal coalescence and breakup. Nevertheless, as thinner ligaments develop, the total liquid mass drops when it should increase.

The analysis presented in this section suggests that achieving good mass-conservation properties and grid

independence in the evolution of the liquid shape becomes a greater challenge than similar VOF codes used in incompressible two-phase flows. Computational cost and physics limit how fine the mesh can be; thus, a compromise between numerical performance, physical coherence (i.e., avoiding a mesh size that enters the non-equilibrium or non-continuum domains) and simulation goals has to be made. If computational cost is not an issue, mesh J3 is preferred in this problem configuration. However, an argument could be made to use mesh J2 in favor of cheaper three-dimensional computations with a similar problem configuration.

6.3.2. Supercritical pressure effects

A brief summary of the main features of liquid injection at supercritical pressures is shown here. The results presented in this section are obtained with mesh J3. Figure 22 presents the distributions of temperature, liquid viscosity, oxygen mass fraction, Y_O , and density on each phase at $t = 4.5 \mu\text{s}$. Moreover, Figure 23 shows the variations along the interface of temperature, oxygen mass fraction in the liquid phase, surface tension coefficient and mass flux per unit area due to phase change.

The characteristics of the mixing process can be seen where the swirling motion captures regions of hotter gas and higher oxygen concentration into the liquid structure. Moreover, the dissolution of the lighter oxygen into the liquid causes a decrease to gas-like values of the liquid viscosity near the interface and a substantial drop in liquid density with respect to liquid core properties. These effects are more pronounced in the elongated liquid structures.

This mixing process is responsible for a faster deformation of the liquid under the shear forces caused by the faster and denser gas, as well as responsible for variations in the interface thermodynamic behavior along the interface. As shown in Figure 23, the surface tension coefficient drops in regions of higher interface temperature due to an enhanced dissolution of oxygen into the liquid. Similarly, the mass flux per unit area also varies. Even though previous tests with simpler configurations at 150 bar only showed net condensation [13, 28, 29], here the deformation of the interface together with mixing allow certain regions of the interface to vaporize. These regions are identified where the hotter gas is compressed (heated) by the liquid motion.

Altogether, the fast growth of the surface instability at high pressures is apparent, which can be linked to a faster atomization later in time. The time scales presented here are similar to those reported in temporal studies of axisymmetric liquid jets [15].

6.4. Three-dimensional planar jet at supercritical pressures

A temporal and symmetric three-dimensional planar jet is presented to further demonstrate the ability of the numerical model to handle three-dimensional configurations. Similar to the two-dimensional case, the jet half-thickness is $H = 10 \mu\text{m}$ and the interface is initially perturbed in the streamwise direction with a sinusoidal wave of $30 \mu\text{m}$ wavelength and $0.5 \mu\text{m}$ amplitude. Another sinusoidal perturbation in the

spanwise direction is superimposed with a $20\ \mu\text{m}$ wavelength and the same $0.5\ \mu\text{m}$ amplitude to enhance three-dimensional effects.

Initially, the liquid is composed of *n*-decane at 450 K and the gas is composed of oxygen at 550 K. The thermodynamic pressure is 150 bar and the streamwise velocity varies with a hyperbolic tangent profile from 0 in the liquid to 30 m/s in the gas. Periodic boundary conditions are imposed in the streamwise and spanwise directions and outflow boundary conditions are imposed in the gas domain boundary away from the interface. Only one wavelength in each direction is enclosed in the computational domain and periodicity in the streamwise and spanwise directions is used when plotting the results.

Only limited three-dimensional results are shown in this paper regarding mesh resolution effects. Figure 24 presents the interface deformation of the three-dimensional planar jet up to $3\ \mu\text{s}$ in time. Two different meshes are used (i.e., J1 and J3) to estimate the effect of mesh size in the development of three-dimensional liquid structures. The liquid surface evolution is practically identical with J1 and J3. Only at $3\ \mu\text{s}$ some deviations can be seen in the elongation of the ligament stretching from the tip of the lobes that form on the liquid surface. The coarser mesh presents thinner and longer ligaments than the finer mesh due to a poorer mesh resolution near the ligament tip. Overall, the rest of the liquid surface looks very similar in both cases, which might justify using mesh J2 instead of mesh J3 to ease the computational cost of three-dimensional simulations.

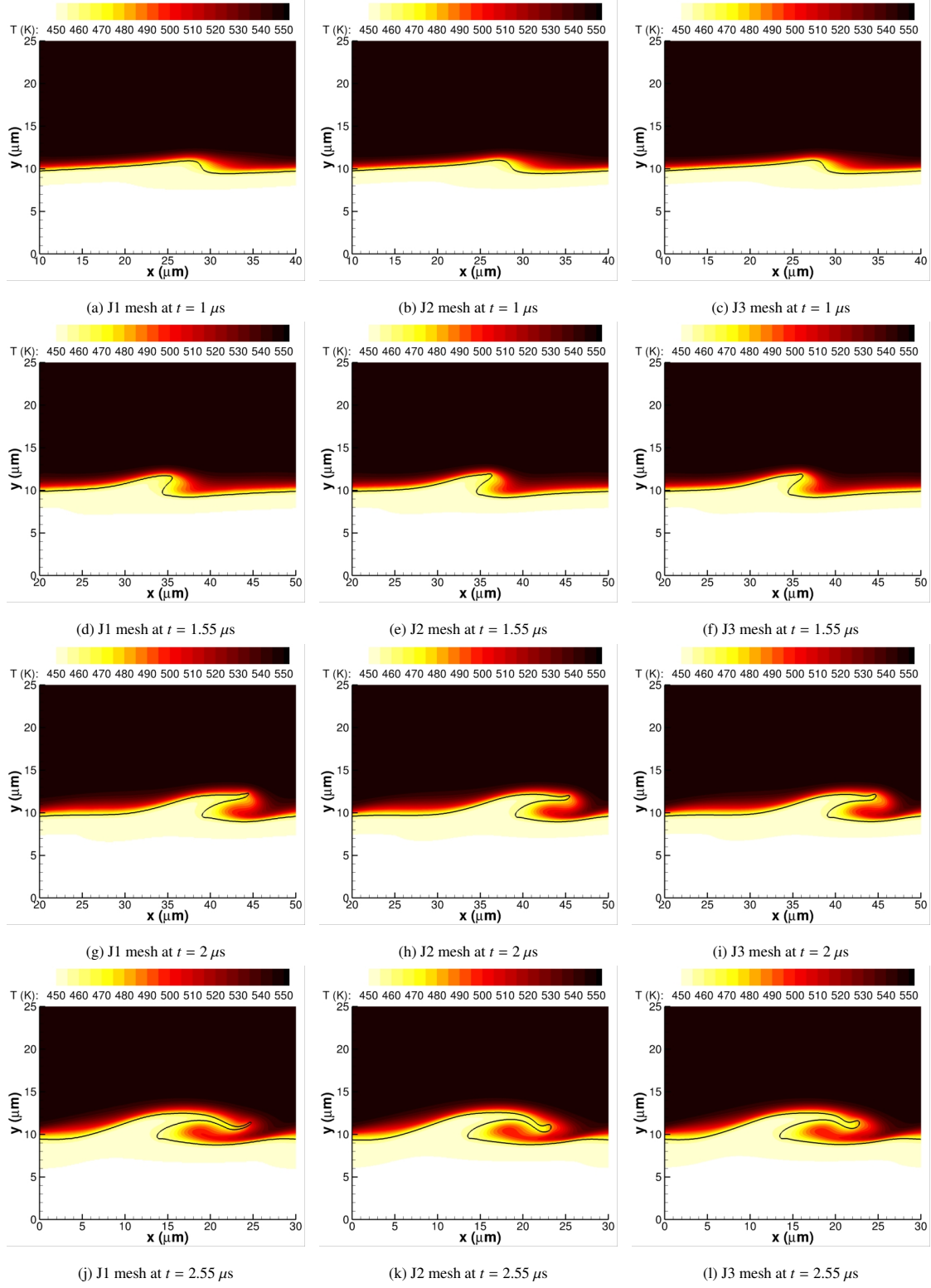


Figure 17: Temperature plots and interface deformation at 150 bar for the two-dimensional planar jet with three mesh sizes J1, J2 and J3. Plotted times correspond to $1 \mu s$, $1.55 \mu s$, $2 \mu s$ and $2.55 \mu s$. The interface location is highlighted with a solid black curve representing the isocontour with $C = 0.5$.

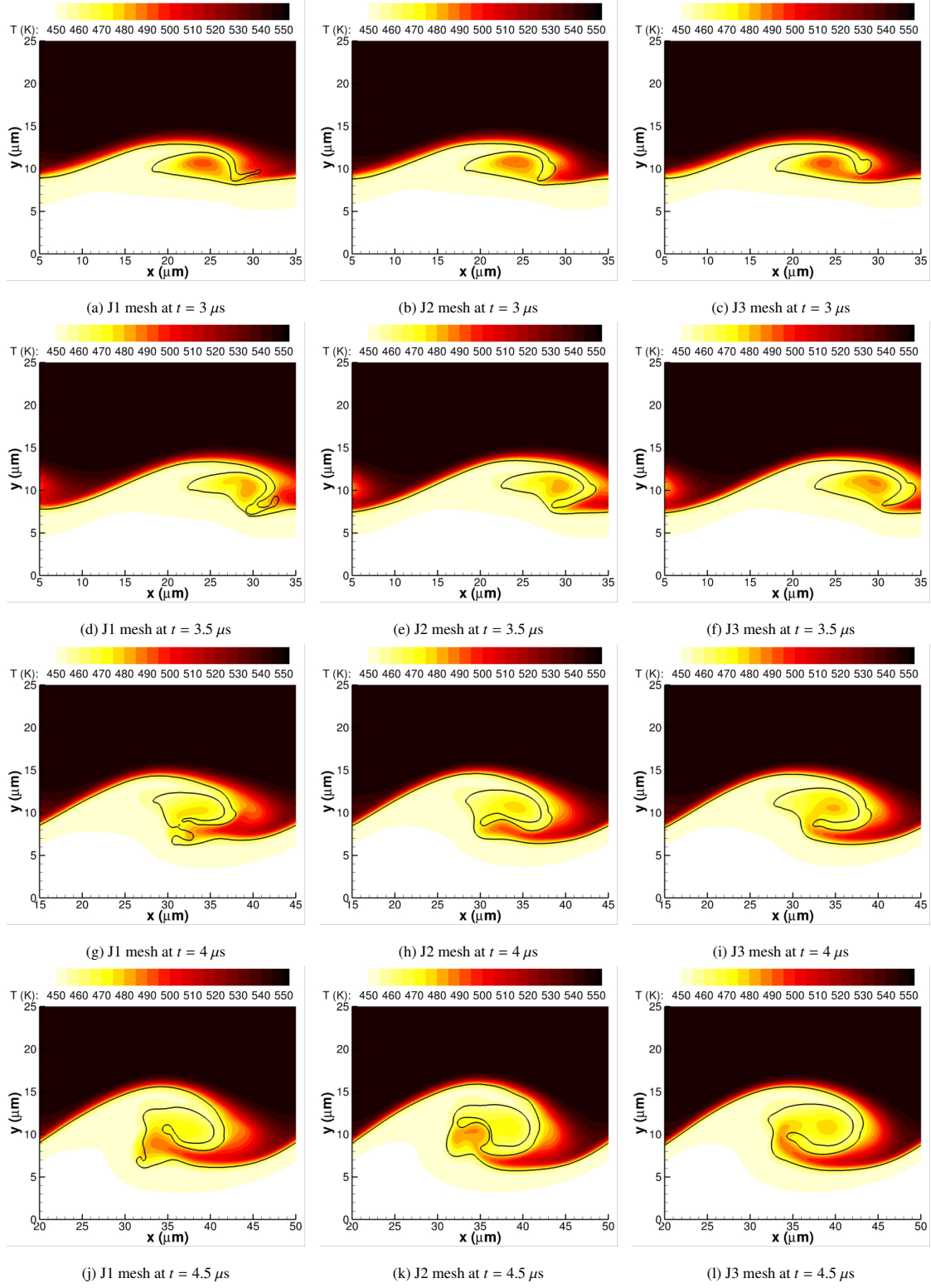


Figure 18: Temperature plots and interface deformation at 150 bar for the two-dimensional planar jet with three mesh sizes J1, J2 and J3. Plotted times correspond to $3 \mu\text{s}$, $3.5 \mu\text{s}$, $4 \mu\text{s}$ and $4.5 \mu\text{s}$. The interface location is highlighted with a solid black curve representing the isocontour with $C = 0.5$.

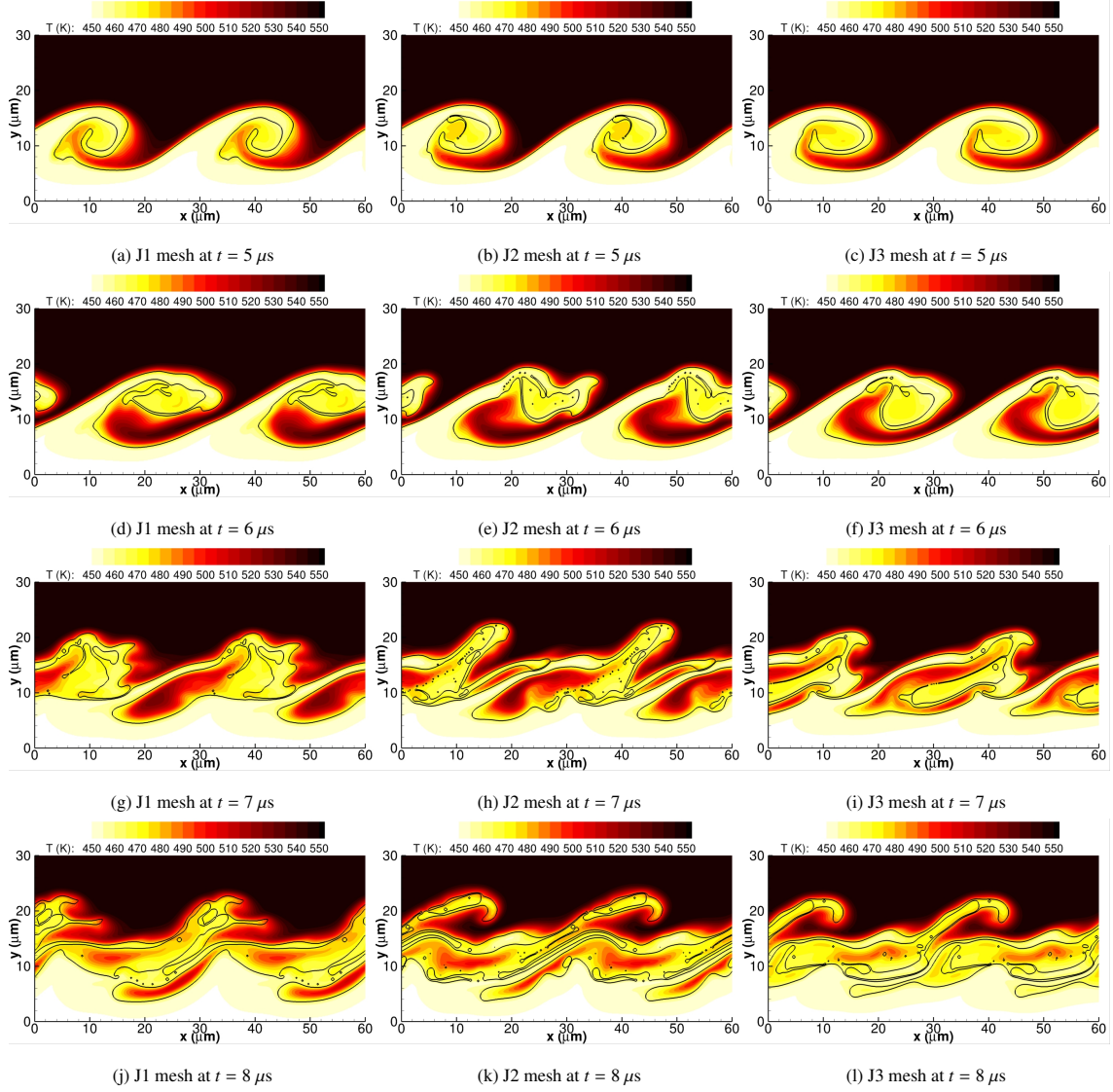
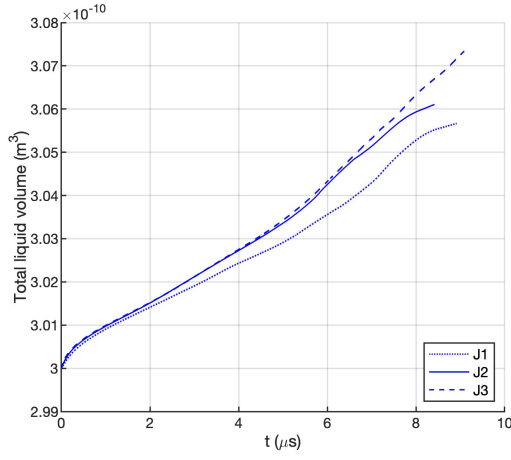
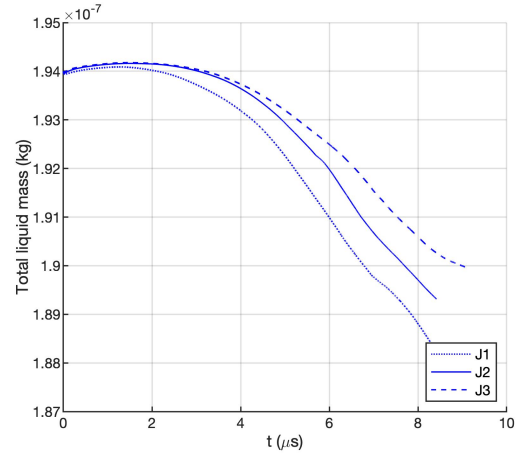


Figure 19: Temperature plots and interface deformation at 150 bar for the two-dimensional planar jet with three mesh sizes J1, J2 and J3. Plotted times correspond to $5 \mu s$, $6 \mu s$, $7 \mu s$ and $8 \mu s$. The interface location is highlighted with a solid black curve representing the isocontour with $C = 0.5$.

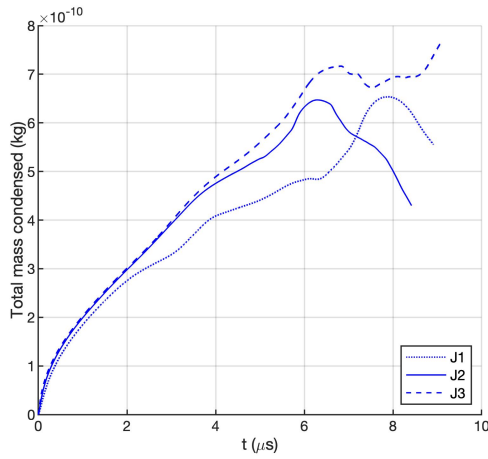


(a)

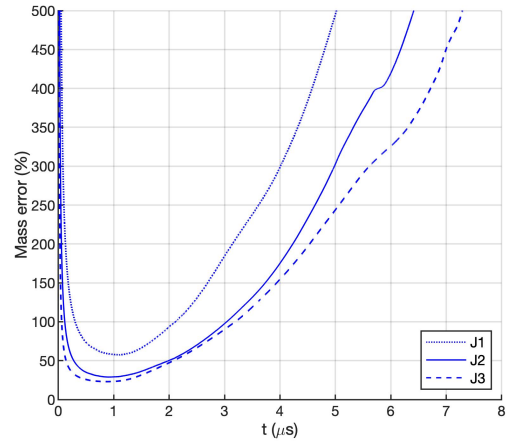


(b)

Figure 20: Temporal evolution of the total liquid volume and the total liquid mass for the two-dimensional planar liquid jet at 150 bar. (a) total liquid volume; (b) total liquid mass.



(a)



(b)

Figure 21: Temporal evolution of the total net mass exchanged across the interface and the estimated mass error for the two-dimensional planar liquid jet at 150 bar. (a) total mass condensed; (b) mass error.

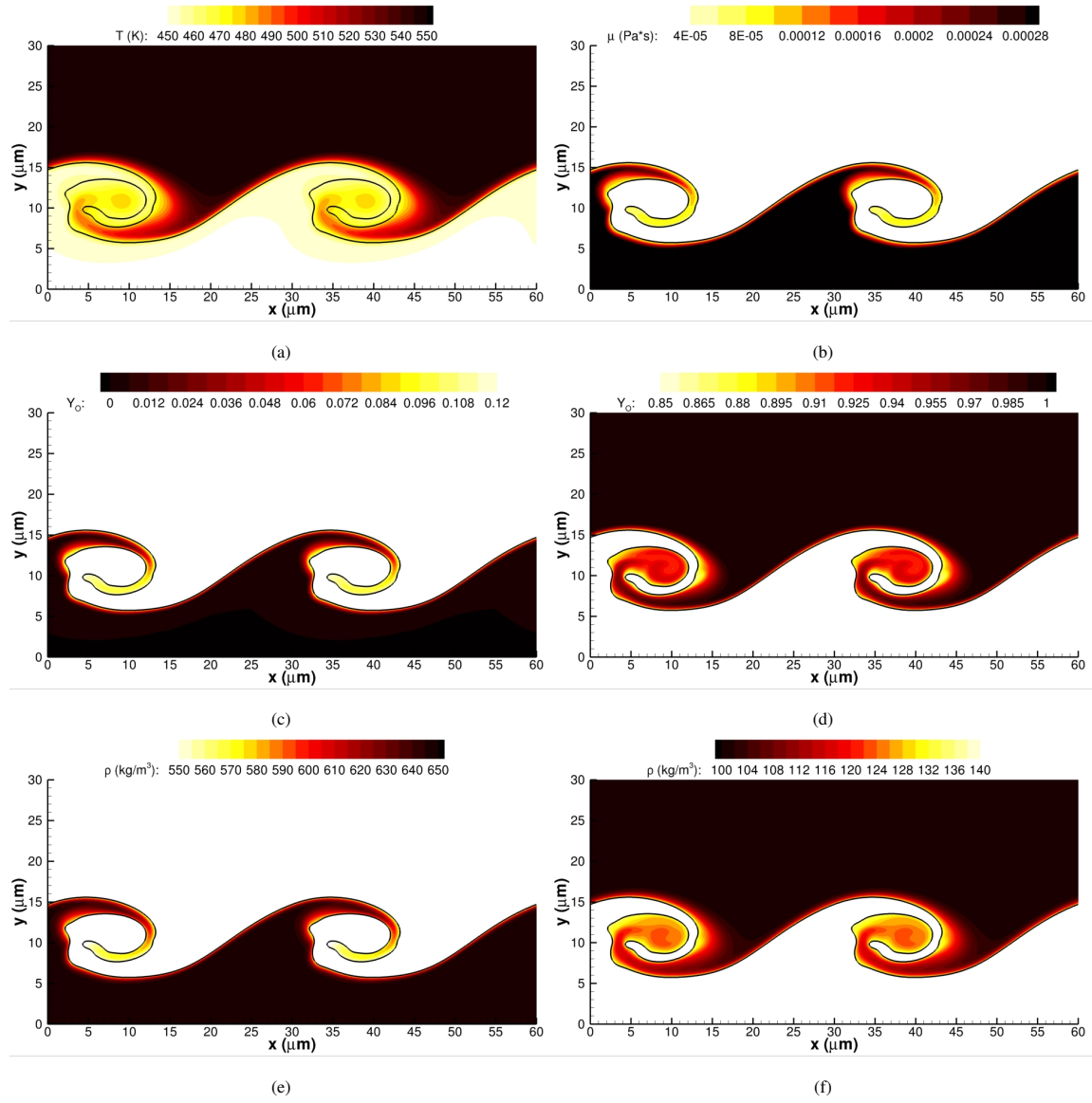


Figure 22: Plots of various variables for the two-dimensional planar jet with mesh J3 at 150 bar and $t = 4.5 \mu\text{s}$. The interface location is highlighted with a solid black curve representing the isocontour with $C = 0.5$. The contour values are chosen to focus on a particular phase in some sub-figures. (a) temperature; (b) liquid viscosity; (c) oxygen mass fraction in the liquid phase; (d) oxygen mass fraction in the gas phase; (e) liquid density; (f) gas density.

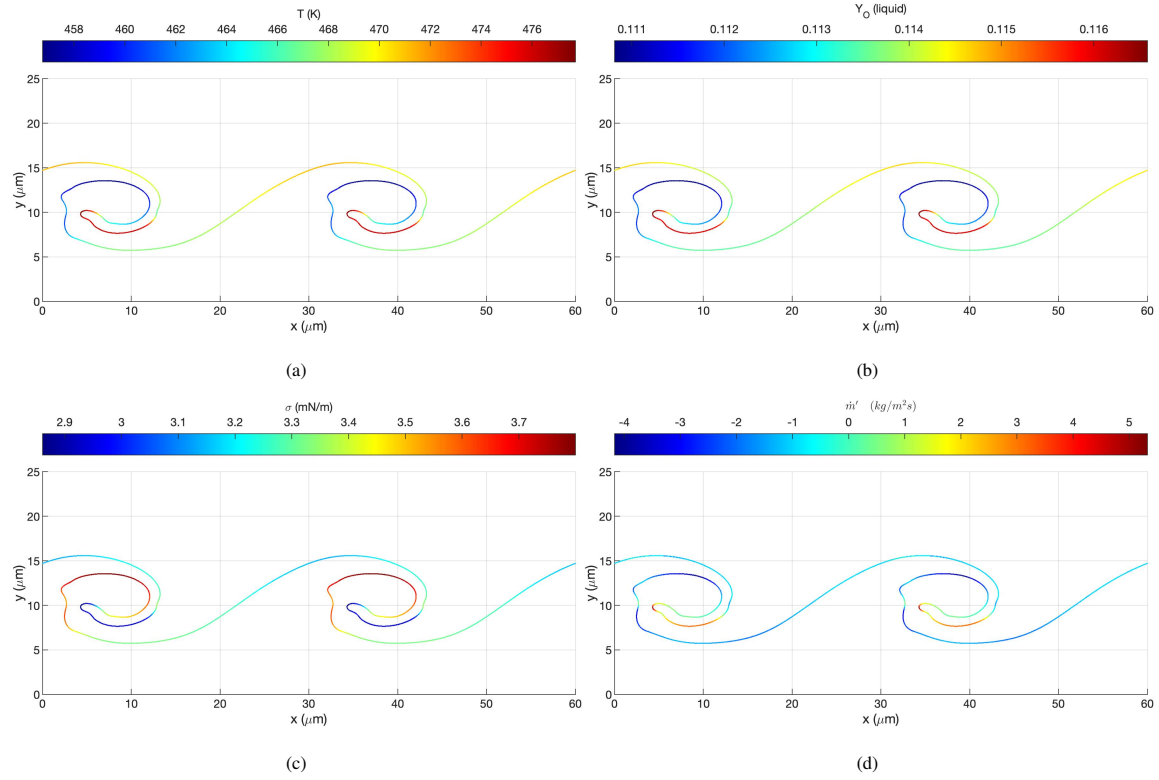


Figure 23: Interface properties for the two-dimensional planar jet with mesh J3 at 150 bar and $t = 4.5 \mu\text{s}$. The interface shape is colored by the value of each variable. (a) temperature; (b) oxygen mass fraction in the liquid phase; (c) surface tension coefficient; (d) mass flux per unit area due to phase change.

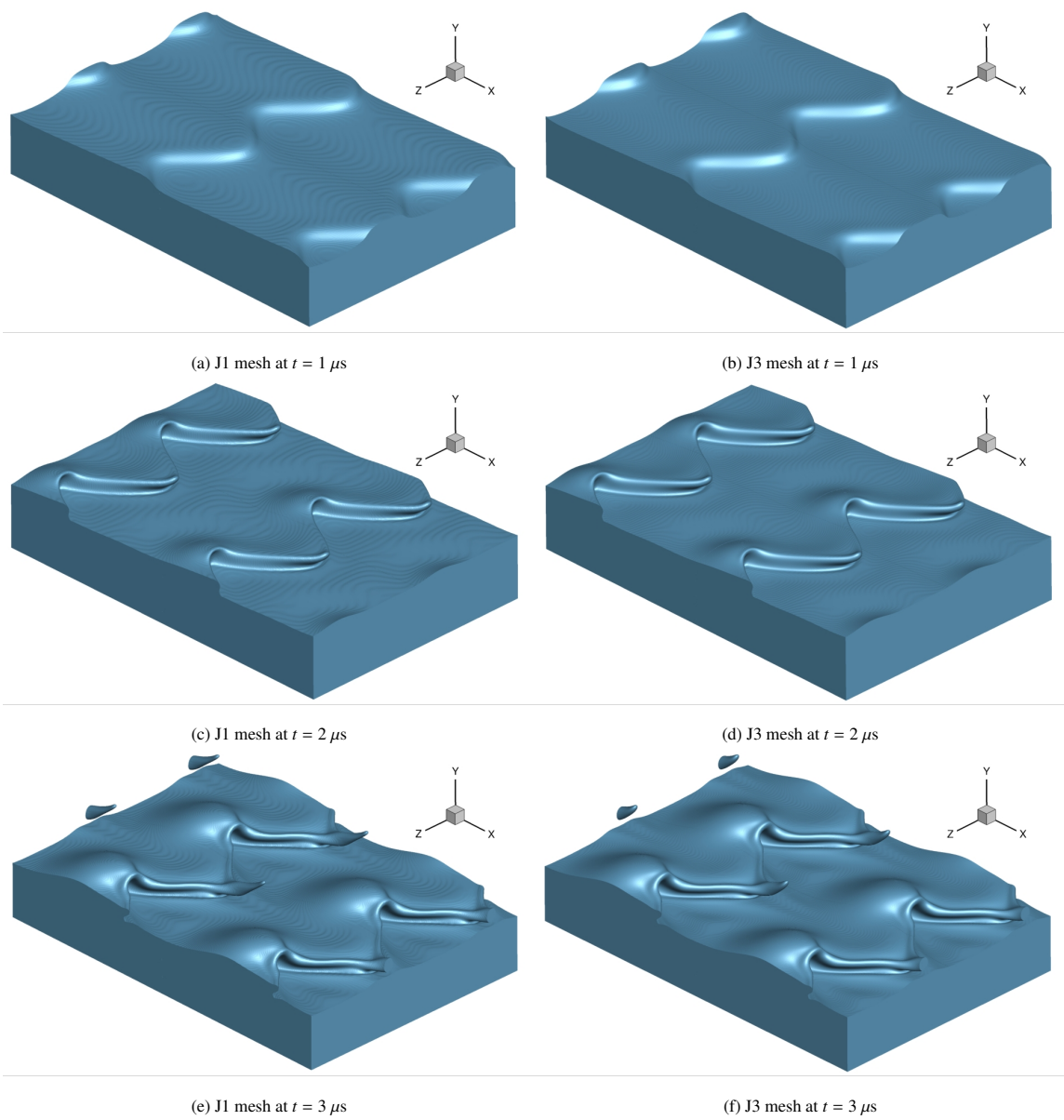


Figure 24: Interface deformation at 150 bar for the three-dimensional planar jet with two mesh sizes J1 and J3.

7. Summary and conclusions

A methodology, both conceptual and numerical, has been presented in this work to solve low-Mach-number compressible two-phase flows. The methodology addresses compressible liquids with phase change and its ultimate goal is the study of supercritical liquid jet injection.

The advection of the liquid phase is performed with an extension of the VOF method from Baraldi et al. [40] to compressible liquids with phase change. Moreover, the low-Mach-number governing equations for two-phase flows, as well as their balancing across the interface, are coupled to a non-ideal thermodynamic model based on the SRK equation of state. Details about this thermodynamic model are available in Davis et al. [28].

The complexity of the model adds extra computational cost. To properly capture the interface properties and its displacement, jump conditions and LTE have to be solved at each interface cell and extrapolations of phase-wise velocity divergences and the corresponding velocity field have to be performed. To alleviate this increase in cost, a constant-coefficient PPE for low-Mach-number flows is developed based on Dodd et al. [41, 42]. This PPE can be solved with an efficient FFT method.

Various tests show the viability and accuracy of the numerical model presented in this work. A sufficiently fine mesh is needed to provide a smooth interface solution and to minimize mass errors. In the limit of incompressible liquid without phase change, the method recovers the mass-conserving properties from [40].

Future works will deal with three-dimensional liquid jets and the analysis of the role of vortex dynamics in the early deformation of the liquid. Additionally, a thermodynamic characterization of the interface will be performed. That is, identifying regions of condensation/vaporization, etc.

Conflict of interest

The authors declared that there is no conflict of interest.

Acknowledgments

The authors are grateful for the helpful discussions in developing this work with Prof. Antonino Ferrante and his student Pablo Trefftz-Posada, from the University of Washington. The incompressible VOF subroutines from his group shared with us are also appreciated. The authors are also grateful for the support of the NSF grant with Award Number 1803833 and Dr. Ron Joslin as Scientific Officer.

References

- [1] W. O. H. Mayer, H. Tamura, Propellant injection in a liquid oxygen/gaseous hydrogen rocket engine, *Journal of Propulsion and Power* 12 (6) (1996) 1137–1147.
- [2] W. O. H. Mayer, A. H. A. Schik, B. Vielle, C. Chauveau, I. Gökalp, D. G. Talley, R. D. Woodward, Atomization and breakup of cryogenic propellants under high-pressure subcritical and supercritical conditions, *Journal of Propulsion and Power* 14 (5) (1998) 835–842.
- [3] W. O. H. Mayer, A. H. A. Schik, M. Schaffler, H. Tamura, Injection and mixing processes in high-pressure liquid oxygen/gaseous hydrogen rocket combustors, *Journal of Propulsion and Power* 16 (5) (2000) 823–828.
- [4] M. Oschwald, J. Smith, R. Branam, J. Hussong, A. Schik, B. Chehroudi, D. G. Talley, Injection of fluids into supercritical environments, *Combustion Science and Technology* 178 (1-3) (2006) 49–100.
- [5] B. Chehroudi, Recent experimental efforts on high-pressure supercritical injection for liquid rockets and their implications, *International Journal of Aerospace Engineering* 2012 (2012) 1–30.
- [6] Z. Falgout, M. Rahm, D. Sedarsky, M. Linne, Gas/fuel jet interfaces under high pressures and temperatures, *Fuel* 168 (2016) 14–21.
- [7] D. Spalding, Theory of particle combustion at high pressures, *ARS Journal* 29 (11) (1959) 828–835.
- [8] D. Rosner, On liquid droplet combustion at high pressures., *AIAA Journal* 5 (1) (1967) 163–166.
- [9] K. C. Hsieh, J. S. Shuen, V. Yang, Droplet vaporization in high-pressure environments I: Near critical conditions, *Combustion Science and Technology* 76 (1-3) (1991) 111–132.
- [10] J.-P. Delplanque, W. A. Sirignano, Numerical study of the transient vaporization of an oxygen droplet at sub- and supercritical conditions, *International Journal of Heat and Mass Transfer* 36 (2) (1993) 303–314.
- [11] V. Yang, J.-S. Shuen, Vaporization of liquid oxygen (LOX) droplets in supercritical hydrogen environments, *Combustion Science and Technology* 97 (4-6) (1994) 247–270.
- [12] W. A. Sirignano, J.-P. Delplanque, F. Liu, Selected challenges in jet and rocket engine combustion research, in: *33rd Joint Propulsion Conference and Exhibit*, 1997, p. 2701.
- [13] J. Poblador-Ibanez, W. A. Sirignano, Transient behavior near liquid-gas interface at supercritical pressure, *International Journal of Heat and Mass Transfer* 126 (2018) 457–473.

- [14] V. Yang, Modeling of supercritical vaporization, mixing, and combustion processes in liquid-fueled propulsion systems, *Proceedings of the Combustion Institute* 28 (1) (2000) 925–942.
- [15] J. Poblador-Ibanez, W. A. Sirignano, Analysis of an axisymmetric liquid jet at supercritical pressures, in: *Proceedings of the ILASS-Americas 30th Annual Conference on Liquid Atomization and Spray Systems*, Tempe, AZ, 2019.
- [16] M. Minniti, A. Ziaee, J. Trolinger, D. Dunn-Rankin, Ultrashort pulse off-axis digital holography for imaging the core structure of transient sprays, *Atomization and Sprays* 28 (6).
- [17] M. Minniti, A. Ziaee, D. Curran, J. Porter, T. Parker, D. Dunn-Rankin, Femtosecond digital holography in the near-nozzle region of a dodecane spray, *Atomization and Sprays* 29 (3) (2019) 251–267.
- [18] C. Traxinger, M. Pfitzner, S. Baab, G. Lamanna, B. Weigand, Experimental and numerical investigation of phase separation due to multicomponent mixing at high-pressure conditions, *Physical Review Fluids* 4 (7) (2019) 074303.
- [19] T. C. Klima, A. Peter, S. Riess, M. Wensing, A. S. Braeuer, Quantification of mixture composition, liquid-phase fraction and temperature in transcritical sprays, *The Journal of Supercritical Fluids* 159 (2020) 104777.
- [20] D. Jarrahbashi, W. A. Sirignano, Vorticity dynamics for transient high-pressure liquid injection, *Physics of Fluids* 26 (10) (2014) 73.
- [21] D. Jarrahbashi, W. A. Sirignano, P. P. Popov, F. Hussain, Early spray development at high gas density: hole, ligament and bridge formations, *Journal of Fluid Mechanics* 792 (2016) 186–231.
- [22] A. Zandian, W. A. Sirignano, F. Hussain, Planar liquid jet: Early deformation and atomization cascades, *Physics of Fluids* 29 (6) (2017) 062109.
- [23] A. Zandian, W. A. Sirignano, F. Hussain, Understanding liquid-jet atomization cascades via vortex dynamics, *Journal of Fluid Mechanics* 843 (2018) 293–354.
- [24] A. Zandian, W. A. Sirignano, F. Hussain, Length-scale cascade and spread rate of atomizing planar liquid jets, *International Journal of Multiphase Flow* 113 (2019) 117–141.
- [25] R. N. Dahms, J. C. Oefelein, On the transition between two-phase and single-phase interface dynamics in multicomponent fluids at supercritical pressures, *Physics of Fluids* 25 (9) (2013) 092103.
- [26] R. N. Dahms, J. C. Oefelein, Liquid jet breakup regimes at supercritical pressures, *Combustion and Flame* 162 (10) (2015) 3648–3657.

- [27] R. N. Dahms, J. C. Oefelein, Non-equilibrium gas-liquid interface dynamics in high-pressure liquid injection systems, *Proceedings of the Combustion Institute* 35 (2) (2015) 1587–1594.
- [28] B. W. Davis, J. Poblador-Ibanez, W. A. Sirignano, Two-phase developing laminar mixing layer at supercritical pressures, *International Journal of Heat and Mass Transfer* 167 (2021) 120687.
- [29] J. Poblador-Ibanez, B. W. Davis, W. A. Sirignano, Self-similar solution of a supercritical two-phase laminar mixing layer, *International Journal of Multiphase Flow* 135 (2021) 103465.
- [30] J. Bellan, Supercritical (and subcritical) fluid behavior and modeling: drops, streams, shear and mixing layers, jets and sprays, *Progress in Energy and Combustion Science* 26 (4-6) (2000) 329–366.
- [31] M. Sussman, P. Smereka, S. Osher, A level set approach for computing solutions to incompressible two-phase flow, *Journal of Computational Physics* 114 (1) (1994) 146–159.
- [32] M. Sussman, E. Fatemi, P. Smereka, S. Osher, An improved level set method for incompressible two-phase flows, *Computers & Fluids* 27 (5-6) (1998) 663–680.
- [33] S. Osher, R. P. Fedkiw, Level set methods: an overview and some recent results, *Journal of Computational Physics* 169 (2) (2001) 463–502.
- [34] C. W. Hirt, B. D. Nichols, Volume of fluid (VOF) method for the dynamics of free boundaries, *Journal of Computational Physics* 39 (1) (1981) 201–225.
- [35] R. Scardovelli, S. Zaleski, Direct numerical simulation of free-surface and interfacial flow, *Annual Review of Fluid Mechanics* 31 (1) (1999) 567–603.
- [36] S. Elghobashi, Direct numerical simulation of turbulent flows laden with droplets or bubbles, *Annual Review of Fluid Mechanics* 51 (2019) 217–244.
- [37] R. P. Fedkiw, T. D. Aslam, B. Merriman, S. Osher, A non-oscillatory Eulerian approach to interfaces in multimaterial flows (the ghost fluid method), *Journal of Computational Physics* 152 (2) (1999) 457–492.
- [38] R. P. Fedkiw, T. D. Aslam, S. Xu, The ghost fluid method for deflagration and detonation discontinuities, *Journal of Computational Physics* 154 (2) (1999) 393–427.
- [39] J.-C. Nave, R. R. Rosales, B. Seibold, A gradient-augmented level set method with an optimally local, coherent advection scheme, *Journal of Computational Physics* 229 (10) (2010) 3802–3827.
- [40] A. Baraldi, M. Dodd, A. Ferrante, A mass-conserving volume-of-fluid method: volume tracking and droplet surface-tension in incompressible isotropic turbulence, *Computers & Fluids* 96 (2014) 322–337.

- [41] M. S. Dodd, A. Ferrante, A fast pressure-correction method for incompressible two-fluid flows, *Journal of Computational Physics* 273 (2014) 416–434.
- [42] M. S. Dodd, P. Trefftz-Posada, A. Ferrante, A coupled volume-of-fluid and pressure-correction method for gas-liquid flows with phase change: I. Incompressible formulation, (In Preparation).
- [43] W. Bo, J. W. Grove, A volume of fluid method based ghost fluid method for compressible multi-fluid flows, *Computers & Fluids* 90 (2014) 113–122.
- [44] B. Duret, R. Canu, J. Reveillon, F. Demoulin, A pressure based method for vaporizing compressible two-phase flows with interface capturing approach, *International Journal of Multiphase Flow* 108 (2018) 42–50.
- [45] F. Jaeger, O. K. Matar, E. A. Müller, Bulk viscosity of molecular fluids, *The Journal of Chemical Physics* 148 (17) (2018) 174504.
- [46] G. Soave, Equilibrium constants from a modified Redlich-Kwong equation of state, *Chemical Engineering Science* 27 (6) (1972) 1197–1203.
- [47] B. E. Poling, J. M. Prausnitz, O. John Paul, R. C. Reid, *The Properties of Gases and Liquids*, Vol. 5, McGraw-Hill New York, 2001.
- [48] R. Stierle, C. Waibel, J. Gross, C. Steinhausen, B. Weigand, G. Lamanna, On the selection of boundary conditions for droplet evaporation and condensation at high pressure and temperature conditions from interfacial transport resistivities, *International Journal of Heat and Mass Transfer* 151 (2020) 119450.
- [49] H. Lin, Y.-Y. Duan, T. Zhang, Z.-M. Huang, Volumetric Property Improvement for the Soave- Redlich-Kwong Equation of State, *Industrial & Engineering Chemistry Research* 45 (5) (2006) 1829–1839.
- [50] J. M. Prausnitz, F. W. Tavares, Thermodynamics of fluid-phase equilibria for standard chemical engineering operations, *AIChE Journal* 50 (4) (2004) 739–761.
- [51] T. H. Chung, M. Ajlan, L. L. Lee, K. E. Starling, Generalized multiparameter correlation for nonpolar and polar fluid transport properties, *Industrial & Engineering Chemistry Research* 27 (4) (1988) 671–679.
- [52] A. Leahy-Dios, A. Firoozabadi, Unified model for nonideal multicomponent molecular diffusion coefficients, *AIChE Journal* 53 (11) (2007) 2932–2939.
- [53] R. Scardovelli, E. Aulisa, S. Manservigi, V. Marra, A marker-VOF algorithm for incompressible flows with interfaces, in: *ASME 2002 Joint US-European Fluids Engineering Division Conference*, American Society of Mechanical Engineers, 2002, pp. 905–910.

- [54] D. L. Youngs, Time-dependent multi-material flow with large fluid distortion, *Numerical Methods for Fluid Dynamics* 1 (1982) 41–51.
- [55] G. Miller, P. Colella, A conservative three-dimensional Eulerian method for coupled solid–fluid shock capturing, *Journal of Computational Physics* 183 (1) (2002) 26–82.
- [56] M. Haghshenas, J. A. Wilson, R. Kumar, Algebraic coupled level set-volume of fluid method for surface tension dominant two-phase flows, *International Journal of Multiphase Flow* 90 (2017) 13–28.
- [57] J. Palmore Jr, O. Desjardins, A volume of fluid framework for interface-resolved simulations of vaporizing liquid-gas flows, *Journal of Computational Physics* 399 (2019) 108954.
- [58] D. J. Harvie, D. F. Fletcher, A new volume of fluid advection algorithm: the stream scheme, *Journal of Computational Physics* 162 (1) (2000) 1–32.
- [59] E. Aulisa, S. Manservigi, R. Scardovelli, S. Zaleski, Interface reconstruction with least-squares fit and split advection in three-dimensional Cartesian geometry, *Journal of Computational Physics* 225 (2) (2007) 2301–2319.
- [60] J. López, C. Zanzi, P. Gómez, R. Zamora, F. Faura, J. Hernández, An improved height function technique for computing interface curvature from volume fractions, *Computer Methods in Applied Mechanics and Engineering* 198 (33–36) (2009) 2555–2564.
- [61] S. Popinet, An accurate adaptive solver for surface-tension-driven interfacial flows, *Journal of Computational Physics* 228 (16) (2009) 5838–5866.
- [62] M. Sussman, E. G. Puckett, A coupled level set and volume-of-fluid method for computing 3D and axisymmetric incompressible two-phase flows, *Journal of Computational Physics* 162 (2) (2000) 301–337.
- [63] M. Sussman, A second order coupled level set and volume-of-fluid method for computing growth and collapse of vapor bubbles, *Journal of Computational Physics* 187 (1) (2003) 110–136.
- [64] M. Herrmann, G. Blanquart, V. Raman, Flux corrected finite volume scheme for preserving scalar boundedness in reacting large-eddy simulations, *AIAA Journal* 44 (12) (2006) 2879–2886.
- [65] G. Tryggvason, J. Lu, Direct numerical simulations of flows with phase change, *Procedia IUTAM* 15 (2015) 2–13.
- [66] T. D. Aslam, A partial differential equation approach to multidimensional extrapolation, *Journal of Computational Physics* 193 (1) (2004) 349–355.

- [67] J. U. Brackbill, D. B. Kothe, C. Zemach, A continuum method for modeling surface tension, *Journal of Computational Physics* 100 (2) (1992) 335–354.
- [68] D. B. Kothe, W. Rider, S. Mosso, J. Brock, J. Hochstein, Volume tracking of interfaces having surface tension in two and three dimensions, in: *34th Aerospace Sciences Meeting and Exhibit*, 1996, p. 859.
- [69] I. Seric, S. Afkhami, L. Kondic, Direct numerical simulation of variable surface tension flows using a volume-of-fluid method, *Journal of Computational Physics* 352 (2018) 615–636.
- [70] A. J. Chorin, A numerical method for solving incompressible viscous flow problems, *Journal of Computational Physics* 2 (1) (1967) 12–26.
- [71] P. Costa, A FFT-based finite-difference solver for massively-parallel direct numerical simulations of turbulent flows, *Computers & Mathematics with Applications* 76 (8) (2018) 1853–1862.
- [72] P. Gaskell, A. Lau, Curvature-compensated convective transport: SMART, a new boundedness-preserving transport algorithm, *International Journal for Numerical Methods in Fluids* 8 (6) (1988) 617–641.
- [73] M. Kang, R. P. Fedkiw, X.-D. Liu, A boundary condition capturing method for multiphase incompressible flow, *Journal of Scientific Computing* 15 (3) (2000) 323–360.
- [74] L. Anumolu, M. F. Trujillo, Gradient augmented level set method for phase change simulations, *Journal of Computational Physics* 353 (2018) 377–406.
- [75] A. Prosperetti, Motion of two superposed viscous fluids, *The Physics of Fluids* 24 (7) (1981) 1217–1223.